Nanoscale Heat Mediators for Magnetic Hyperthermia: Materials, Problems, and Prospects

Alexandr Tovstolytkin, Anatolii Belous, Yaryna Lytvynenko, Yuliia Shlapa, Serhii Solopan, and Larissa Bubnovskaya

1 Overview

1.1 Motivation and Significance of the Problem Under Study

Among the pressing issues of our time, a special place belongs to the problem of the fight against cancer diseases, in particular with deeply located tumors. Diseases of this type cause fear and association with the death fate, although in reality it is only a diagnosis, and most cancers in the early stages of detection are treatable. The incredibly disturbing is the fast increase in cancer incidence around the world. According to the data of the World Health Organization (WHO) [1] in the absence of new methods of treatment, the number of cancer cases can grow from 19 million people in 2020 to 29.5 million until 2040. At the same time, the cancer death rate is growing too. As claimed by the same prediction of WHO [1], the estimated number of deaths due to oncological diseases during this period will increase by 71.5%: from 10.1 million people in 2020 to 16.4 million in 2040. Until 2040 a significant growth of the mortality rate is expected in African countries (>100%) and Asia (~77%), and slightly less in North America (~59%) and Europe (~32%). Therefore,

A. Tovstolytkin (✉) · Y. Lytvynenko
Institute of Magnetism of the NAS of Ukraine and MES of Ukraine, Kyiv, Ukraine
e-mail: atov@imag.kiev.ua

A. Belous · Y. Shlapa · S. Solopan
V.I. Vernadsky Institute of General and Inorganic Chemistry of the NAS of Ukraine, Kyiv, Ukraine
e-mail: belous@ionc.kiev.ua

L. Bubnovskaya
R.E. Kavetsky Institute of Experimental Pathology, Oncology and Radiobiology of the NAS of Ukraine, Kyiv, Ukraine

the instant task is to improve already existing methods of diagnosis and treatment of the oncological diseases, particularly those with deeply located tumors, as well as developing the new ones.

1.2   Progress in Cancer Treatment and Current Challenges

Nowadays, there are powerful methods of fighting oncological tumors, such as surgery, chemotherapy, and radiation therapy (radiotherapy). The two of the last methods are characterized by high efficiency, but at the same time, they are "aggressive" with many side effects that negatively affect the normal functioning of the body and the quality of life in general. In the case of chemotherapy, the injected drugs are spread throughout the body and it is necessary to apply "huge" doses to achieve the desired concentration of the drug in the tumor area. This has a devastating effect not only on malignant formations but also on healthy organs, which significantly suppresses their vital activity. For this reason, quite often a patient must stop the drug treatment only to save the body from full destruction. At the same time, the radiation doses received during radiotherapy affect both the tumor itself and healthy tissues in its vicinity. This brings up the important questions: "Is it possible to focus the therapeutic effect only on a tumor? And how can harmful side effects be reduced?". The technological progress provides an answer to these questions—magnetic hyperthermia (MHT) is one of the promising and safe methods with the opportunity to localize the effect only on the malignant formation and is gradually being introduced into world medical practice.

The principle of MHT is based on the well-known fact that cancer cells are more sensitive to the heat than healthy body tissues. In particular, it is known that heating to 42–45 °C increases the sensitivity of the affected cells to chemotherapy or radiotherapy. In this case, the doses of drugs or irradiation can be significantly lowered (twice or even three times compared to the independent use of these methods); consequently, MHT allows reduction of the side effects. Also, cancer cells can be destroyed by heating to 46–50 °C (in medicine it is known as thermoablation).

MHT consists of three important stages: the first—injection of magnetic nanoparticles (magnetic fluids) and their localization in the tumor area; the second—nanoparticle heating in an external alternating magnetic field (AMF); and the third—the use of chemotherapy or radiotherapy when reaching and maintaining a temperature of 42–45 °C, or further heating of the tissues to the temperature of the destruction of cancer cells at 46–50 °C (thermoablation). Thus, magnetic nanoparticles play the role of heat mediators, which locally heat their environment (tumor) to the required temperature providing the desired therapeutic effect.

There are several advantages of magnetic hyperthermia over other methods of cancer treatment. Firstly, the location of the nanoparticles can be effectively controlled by the magnetic field that allows them to concentrate and held in the tumor area. Secondly, the use of magnetic hyperthermia makes it possible to treat deeply

located tumors with little or no surgery. Third, the benefits include almost complete absence of the side effects of treatment.

2 Self-Controlled Magnetic Hyperthermia: Ideas and Approaches

Magnetic hyperthermia still has many unresolved issues on its way to wide usage. Important among them is the problem of reliable temperature control in the tumor area and beyond (to avoid overheating of healthy tissues), as well as achieving a uniform temperature distribution in the tumor volume.

The optimal temperature interval for the destruction of malignant tumors is 42–45 °C (46–50 °C for the case of thermoablation) [2, 3]. The problem of uneven heating of the tumor in the absence of the risk of overheating and damage to healthy tissues of the body can be solved when used as an heat mediator of MHT substances for which the phase transition from magnetic to nonmagnetic state (Curie temperature T_C) slightly exceeds the above ranges. In this case, when it reaches a temperature close to T_C, heat dissipation in the tumor containing magnetic nanoparticles is automatically stopped. This eliminates the need for precise control of the tumor temperature (since the placement of temperature sensors in the tumor is often simply impossible), as well as the power of electromagnetic radiation. Such approach also allows avoiding the risk of overheating and the associated with it subsequent damage to healthy tissues, as well as skin burns over the tumor. If necessary, this will make it possible to increase the "heat dose" by increasing the time of hyperthermal exposure. As a result, the tumors are evenly warmed up, including deeply located ones.

Currently, the most common magnetic materials for the heating of tumors and targeted drug delivery are magnetite (Fe_3O_4) and maghemite (γ-Fe_2O_3), which crystallize in a spinel structure and whose biocompatibility is well established. However, they have relatively high Curie temperatures (near or above 500 °C), which prevents them from being used in self-controlled MHT [4–7].

To uniformly heat the tumor in the absence of risk of overheating and damage to healthy body tissues, there are very promising nanoparticles developed based on strontium-substituted lanthanum manganite (La, Sr)MnO_3, which are characterized by the structure of deformed perovskite and ferromagnetism with Curie temperature T_C in the range 30–77 °C, where the latter can be tuned by changing the chemical composition and synthesis conditions. Also, magnetic materials with relatively low Curie temperature can be obtained from solid solutions with spinel structure, for example, nickel–zinc ferrite $Ni_{1-x}Zn_xMn_2O_4$.

Thus, there are several groups of nanomaterials, which are currently attracting the attention of scientists:

1. Materials *requiring external temperature control* at the time of MHT:

1.1. Ferrimagnetic spinels AFe_2O_4 (A = Fe, Ni, Mn, Co, Zn, etc.), which may have a wide range of magnetic properties due to variations in chemical composition and method of preparation [6, 8–10]. The advantages of spinel ferrites are the relatively high saturation magnetization and high chemical stability, as well as the opportunity of making an almost unlimited number of solid solutions.

1.2. Composite nanostructures, in particular those that combine soft and hard magnetic materials in core/shell nanoparticles. By combining the high saturation magnetization of soft material with the high coercivity of a hard material, it is possible to achieve the parameters overcoming those of the individual counterparts [11–14]. In this context, attention should be paid to the spinel ferrite materials due to the same crystallographic structure and almost negligible lattice mismatch, and a wide range of magnetic properties.

2. Materials with *automatic preset temperature control*, which include the following:

2.1. Solid solutions based on the ferrites with spinel structure and relatively low Curie temperature, particularly nickel–zinc ferrites $Ni_{1-x}Zn_xMn_2O_4$ [15–17].

2.2. The lanthanum–strontium manganites (La, Sr)MnO_3 with structures of perovskite. These materials have a moderate coefficient of heating in an alternating magnetic field and exhibit an easily controlled Curie temperature near the range optimal for magnetic hyperthermia [18–21].

3 Techniques for the Synthesis of Magnetic Nanoparticles

3.1 Basic Characteristics of the Heat Mediators for the Hyperthermia

Magnetic nanoparticles have to satisfy a number of requirements to be used as the heat mediators of MHT. First of all, they must meet biomedical requirements (nontoxicity, biocompatibility with living organisms, etc.). In particular, they should have certain parameters regarding cytotoxicity, genotoxicity, antioxidant, and antiviral activity [10, 22]. The size of the nanoparticles also plays a significant role: It should be in the range from 10 to 100 nm—the smaller particles are quickly removed by renal clearance, while the bigger ones are taken up by liver and spleen [23–26].

Along with the need to meet the biomedical requirements, the MHT heat mediators should have high heating efficiency under the influence of AMF with certain parameters. A quantitative measure of heating efficiency is specific loss power (SLP; also referred to as the specific absorption rate, SAR). SLP represents the energy loss of the AMF per unit time, normalized per unit mass of magnetic nanoparticles (MNPs) [18, 27].

It should be noted that some limitations also apply to the magnetic field parameters used to heat the nanoparticles. On the one hand, the heating efficiency of the nanoparticles increases with the increase in amplitude and frequency of the AMF. But on the other hand, medical restrictions are imposed on the values of these parameters for the safe effect of the field on normal tissues of the body. Thus, the frequency f should not exceed several MHz, and the product of the magnetic field amplitude by the frequency, $H_{max} f$, should be less than 5×10^9 A·m^{-1}·s^{-1} [10, 18].

As a result, the magnetic nanoparticles used as heat mediators in the hyperthermia must meet the stringent criteria: (1) They have to be made (or coated) of nontoxic biocompatible material, (2) not stick together to ensure homogeneous distribution in the tumor and prevent thrombus formation, (3) be less than 100 nm in size for effective cell penetration, and, at the same time, (4) be characterized by efficient heating in an alternating magnetic field.

3.2   Methods of Synthesis: Advantages and Drawbacks

To prepare the nanoparticles (NPs), it is necessary to choose the methods of synthesis, which would satisfy the previously presented requirements. However, different materials acquire different properties at the same conditions of synthesis; therefore, *there are no sole (universal) methods of synthesis*, which would be able to allow preparing the nanostructures with desired (predefined) properties.

One of the features, which plays an important role during choosing the method and conditions of synthesis, is the energy of the formation of crystalline structure. According to the literature data [28], the energy of formation for the spinel structure equals approximately 30–60 kJ/mol that is much less than for the perovskite structure, for example. Due to this fact, nanosized weakly agglomerated crystalline NPs of the materials with the spinel structure can be obtained during the synthesis process *at relatively low temperatures*. It allows the *crystalline* NPs of materials with the spinel structure during the synthesis *without additional heat treatment*.

At the same time, such a method of synthesis does not allow obtaining the crystalline NPs of perovskites since the energy of the formation of the crystalline structure for them is much higher [29]. Therefore, an *amorphous* precipitate is formed during the synthesis of NPs with the perovskite structure in solutions independently on the method; to obtain *the crystalline* particles, it is necessary to carry out *additional heat treatment*, which results in the growth of NPs and their significant agglomeration.

Structure and properties of (La, Sr)MnO$_3$ manganite NPs, which crystallize in the perovskite structure, are sensitive to the conditions and methods of synthesis, and it is necessary to perform the synthesis in solutions to obtain them in nanoscale form. It is known that the temperature of formation of single-phase crystalline product is higher than 1000 °C during the synthesis of manganite NPs in aqueous solutions that leads to the growth and agglomeration of the particles [30]. Therefore, the methods of synthesis with using *the nonaqueous solutions and organic compounds*

can be promising because they can allow blocking the interactions between individual particles in contrast to the NPs synthesized in an aqueous medium.

Consequently, taking into account the features of the crystalline structure, *several methods* were chosen for the synthesis of magnetic NPs with the spinel and perovskite structures: synthesis via cryochemical method, precipitation in microemulsions and nonaqueous solutions, hydroxide precipitation, and solgel method.

3.3 Synthesis of Weakly Agglomerated Nanoparticles of Ferrispinels AFe_2O_4 (A = Fe, Ni, Co, Mn, Zn)

To synthesize the NPs with the spinel structure by the precipitation methods, aqueous solutions of metal salts $FeCl_3$, $FeSO_4$, $Ni(NO_3)_2$, and $Zn(NO_3)_2$ were used as the starting reagents and solutions of ammonia or sodium hydroxide as the precipitators. Oleic acid was used for the stabilization of synthesized NPs.

Synthesis of Fe_3O_4 NPs via cryochemical method was performed in the closed system in the argon atmosphere according to the technique described in [31]. The solution, which contained the stoichiometric amount of $FeSO_4$ and $FeCl_3$ salts, was frozen using the liquid nitrogen up to the formation of ice, which was placed into the aqueous solution of ammonia under the intensive stirring to the formation of the black mixture. The obtained mixture was stirred for 20 min at 20–30 °C. Formed NPs were separated and washed with the bidistilled water. Prepared product was dispersed in the ethanol; oleic acid was added to the solution, and it was stirred for 2 h at 50 °C. NPs coated with the oleic acid were decanted, washed with ethanol, and dispersed in the necessary volume of water.

As it was established by TEM microscopy, synthesized NPs were weakly agglomerated with the average size of 10–15 nm and narrow size distribution.

Synthesis of Fe_3O_4 NPs in the reverse microemulsions was performed according to the scheme presented in [31, 32]. To prepare the reverse microemulsions, it used the necessary surfactant (Triton X–100, Brij–35 or CTAB), n-butanol as an additional surfactant, cyclohexane as a solvent, and corresponding aqueous phase. The aqueous phase of the first microemulsion consisted of the necessary amount of iron salts and the aqueous phase of the second one–the solution of precipitator (ammonia). To perform the synthesis, microemulsions of salts and precipitators were mixed for 1 h with further intensive stirring and heating at 70 °C for 3 h. Precipitated NPs were separated by centrifugation and washed with ethanol and bidistilled water.

TEM microscopy data showed that such a method of synthesis allowed obtaining nanosized weakly agglomerated particles, which sizes could be varied in the range from 4–8 to 10–20 nm by using different surfactants for preparation of the microemulsions.

Synthesis of NPs with the spinel structure in the solution of diethylene glycol (DEG) was performed as described in Refs. [33–36]. For synthesis, stoichiometric amounts of metal salts ($FeSO_4$ or $A(NO_3)_2$) and $Fe(NO_3)_3$ were dissolved in DEG

and stirred for 1 h; simultaneously, the solution of NaOH in DEG was prepared. The alkaline solution was added by drops to the mixture of salts with constant stirring for 4 h. The obtained solution was heated at 200–220 °C for 60 min; after this, the solution of oleic acid in DEG was added to the reaction mixture and stirred for 1 h. Formation of the NPs of AFe_2O_4 compounds was observed during the cooling the mixture to the room temperature, and they were washed from the impurities by dispersing in ethanol with further centrifugation. NPs were saved in the solution or dried in the air at 30–50 °C for further investigations.

As it was established by TEM, this method of synthesis provided the obtaining nanosized weakly agglomerated particles with size of 4–9 nm.

3.4   Synthesis of Core/Shell Structures $Fe_3O_4/CoFe_2O_4$

Synthesis of core/shell structures $Fe_3O_4/CoFe_2O_4$ was performed according to the technique presented in [14, 37]. Fe_3O_4 synthesized by the precipitation in diethylene glycol without the addition of the oleic acid was used as a core. The synthesis of the shell was performed in the argon atmosphere. Necessary amounts of cobalt and iron nitrates were dissolved in DEG and stirred for 1 h. The solution of precipitator NaOH in DEG was prepared separately, and it was added to the solution of salts with stirring for 2 h. Previously synthesized Fe_3O_4 NPs were put into the solution and stirred for 2 h. The reaction mixture was heated up at 200–220 °C for 90 min reaching the desired temperature for 1.5 h. When the heat treatment finished, oleic acid was added with further stirring of the reaction mass up to cooling. Synthesized NPs were washed with the water–alcohol solution; the precipitate was separated by centrifugation. During the synthesis of core/shell structures, it was considered that Fe_3O_4 NPs (core) had a spherical shape with an average size of 6.3 nm [33], on which different amounts of $CoFe_2O_4$ was precipitated. The volume of the coating $CoFe_2O_4$ (shell) was calculated according to [14] using the equation $V = 4/3*\pi*((R_2)^3-(R_1)^3)$ (R_1 and R_2—radii of starting and coated spherical particle, respectively) and taking into account that $m = \rho \cdot V$ (m—mass, ρ—density of the material of core or shell).

3.5   Synthesis of Solid Solutions of $Ni_{1-x}Zn_xMn_2O_4$ with the Spinel Structure

Synthesis of NPs of solid solutions of $Ni_{1-x}Zn_xMn_2O_4$ ($x = 0$; 0.25; 0.50; 0.75; 0.80; 0.85; 0.90; 0.95; 1.00) by precipitation in the aqueous solutions was performed according to the technique described in [15]. As it was shown, the amorphous precursors formed during the synthesis process at 80 °C; therefore, these precursors were subjected to the heat treatment at 800 °C for 2 h. The main advantages of this

method are its simplicity, low cost, and the possibility to synthesize a large amount of the final product. However, high-temperature treatment of the powder leads to the growth and agglomeration of NPs that is the drawback for their practical application, particularly in medicine.

3.6 Synthesis and Properties of Nanosized Particles Based on (La, Sr)MnO₃

Synthesis of (La, Sr)MnO₃ (LSMO) NPs by precipitation in the nonaqueous solutions. A solid solution of $(La, Sr)MnO_3$ manganite is quite complex system since it consists of the ions of three different metals—La, Sr, and Mn. As it is known, all of them precipitate in the aqueous solutions at different pH values that make the synthesis more complicated [30]. Therefore, the synthesis of LSMO NPs by precipitation in the nonaqueous solutions can be more satisfactory in terms of the choice of the conditions for synthesis. Usually, polyhydric alcohols, namely glycols (for example diethylene glycol DEG), are chosen as a medium for synthesis. It is due to several important factors: (1) application of glycols allows performing the coprecipitation of the metal cations, which have a large difference in pH values for the precipitation in the aqueous solution; (2) as the polyhydric alcohol, DEG can react with the metal cations; therefore, it can affect the synthesis process and stabilization of NPs; (3) DEG has the relatively high viscosity that allows avoiding the interaction between NPs during the precipitation process.

Synthesis of manganite NPs by precipitation in DEG solution was performed according to the technique described in detail in [38]. The solution, which contained the stoichiometric amounts of metal nitrates in DEG, was heated up to 200 °C in the argon atmosphere; then, the solution of NaOH in DEG was added by drops to the reaction mixture with constant stirring. The obtained reaction system was stirred and heated up on the oil bath at 200–220 °C for 1 h. After the heating was finished, the solution of oleic acid in DEG was added to the system, and it was left for cooling to the room temperature with stirring. Particles were separated by centrifugation and dispersed in ethanol. An obtained precursor was dried in the air at 30–50 °C, and to obtain crystalline NPs, this precursor was subjected to the heat treatment at 800 °C.

Synthesis of La₁₋ₓSrₓMnO₃ NPs by precipitation in reverse microemulsions. Synthesis of manganite NPs by precipitation in the reverse microemulsions was performed as described in [39]. It is known that the structure and nature of the surfactant can significantly affect the size and properties of synthesized NPs [40]. One more important thing for obtaining LSMO NPs is that it is necessary to choose surfactants, which do not contain any metal ions. It is connected with the fact that such ions can additionally incorporate into the structure during the heat treatment of the nonmagnetic precursor and it can result in a significant change of the properties (particularly, magnetic ones) of the final crystalline product. Therefore,

microemulsions were prepared based on three different surfactants: Triton X-100, CTAB, and Brij-35.

To synthesis LSMO NPs via this method, it was prepared two microemulsions (M1 and M2), which consisted of corresponding surfactant (CTAB, Triton X-100 or Brij-35), n-butanol as cosurfactant, cyclohexane, and aqueous solution. The aqueous phase of M1 contained metal salts, and the aqueous phase of M2 contained the solution of the precipitator (NH_3). M2 was added to M1 dropwise for 1 h with further heating the mixture at 70 °C for 1 h. Precipitated NPs were separated by centrifugation, and then they were washed with ethanol and bidistilled water for several times by desperation and centrifugation. To obtain crystalline NPs, corresponding amorphous precursors were subjected to the high-temperature treatment at 800 °C for 2 h.

When LSMO NPs were synthesized via a solgel method, water-soluble salts $La(NO_3)_3$, $Mn(NO_3)_2$, and $Sr(NO_3)_2$ were used as the starting reagents [41–47]. Necessary molar amounts of salts were dissolved in bidistilled water, and gel-formed agents, citric acid and ethylene glycol, were added to this solution. The obtained mixture was heated up at 80 °C with stirring, polyesterification reaction took place, and polymer gel was formed. Pyrolysis of the gel was at 200 °C, and precursor powder was obtained as a result of pyrolysis [48]. This precursor was subjected to further mechanochemical treatment using different approaches: (1) heat treatment at 800 °C for 2 h; (2) grinding with alcohol and heat treatment at 800 °C for 2 h; (3) grinding with alcohol and further three-stage heat treatment at 400 °C, 600 °C, and 800 °C for 2 h; (4) grinding in the mill and heat treatment at 800 °C for 2 h; (5) effect of ultrasonication for 3 h with further heat treatment at 800 °C for 2 h; (6) pressing into the tablet with further heat treatment at 800 °C for 2 h; (7) heat treatment at 600 °C for 10 h; (8) grinding with the ammonium nitrate with further heat treatment at 800 °C for 2 h.

It is important to note that the application of different methods of mechanochemical treatment of the precursor after solgel synthesis allows obtaining NPs with different size and size distribution. However, considering some methodological features of synthesis and treatment of obtained particles [49], this method allows decreasing the size of NPs to 35 nm and obtaining relatively weakly agglomerated manganite NPs.

As it was shown by X-ray diffraction data, nonmagnetic amorphous precursors formed after synthesis via all three methods. It was established that when manganite NPs were synthesized by methods using organic compounds and nonaqueous medium, single-phase crystalline structure began to form in one stage at 600° and it completely formed at 800 °C.

Results of microstructural studies of manganite NPs showed that their size and morphology significantly depended on the method and conditions of synthesis. It was established that manganite NPs synthesized via three different methods had the average sizes in the range of 20–40 nm with narrow size distribution [39].

It follows from the above-considered data that there is *no unique method* to synthesize MNPs with reliably tunable and reproducible parameters. On the contrary, each specific material with certain properties needs a thoroughly adapted

fabrication technique. The main characteristics of the techniques we employed in this work for the fabrication of MNPs with the spinel and perovskite structural types are presented in Table 1.

4 Materials Requiring External Temperature Control when Used in MHT

4.1 Ferrimagnetic Spinels AFe_2O_4 (A = Fe, Ni, Mn, Co, Zn, etc.)

Synthesis of nanoparticles was carried out by precipitation in diethylene glycol solutions (Fe1), by cryochemical method (Fe2) and in microemulsion using Triton X-100 (Fe3), Brij-35 (Fe4) and CTAB (Fe5) as surfactants [31]. The X-ray diffraction revealed that the nanoparticles obtained were characterized by a cubic spinel crystal structure (JCPDS Card Number 19-0629 [50]) (Fig. 1). Also, the diffraction patterns of samples Fe3, Fe4, and Fe5 showed an additional phase of goethite FeOOH [50]. As can be estimated from the results of the TEM study (Fig. 1), synthesized nanoparticles are nanosized and characterized by weak agglomeration. The mean diameter of NPs varies from 6 to 15 nm depending on the method of synthesis.

Magnetic measurements for synthesized nanoparticles were performed at the temperatures 300 and 10 K. As shown in Fig. 2, in both cases, magnetization tends to saturation at the high fields. Magnetic parameters are collected in Table 2.
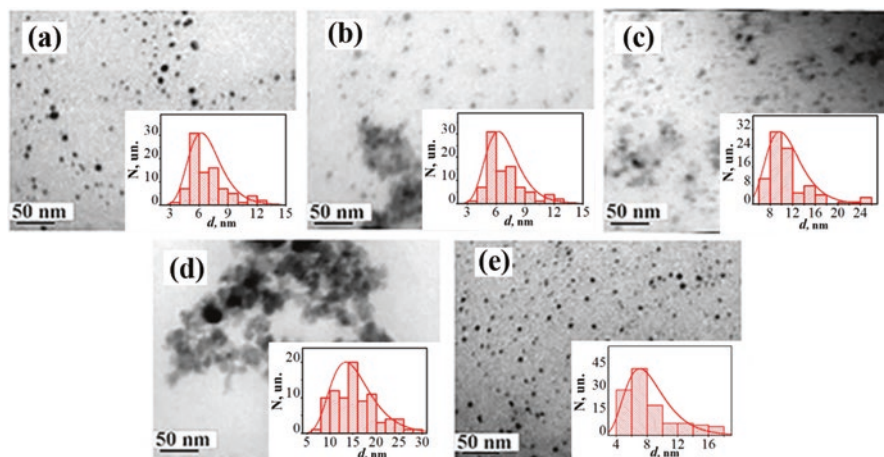
Fig. 1 TEM images of nanoparticles synthesized by various methods: (**a**) Fe1; (**b**) Fe2; (**c**) Fe3; (**d**) Fe4; (**e**) Fe5. Insets show the diagrams of size distribution for corresponding ensembles of nanoparticles

Table 1 Characterization of different techniques employed in this work to synthesize MNPs with the parameters tailored for MHT

Synthesis method	MNPs with a spinel structural type		MNPs with a perovskite structural type	
	Advantages	Disadvantages	Advantages	Disadvantages
Cryochemical method	A possibility to synthesize a large amount of MNPs. The particles are weakly agglomerated and nanosized. Relatively high heating efficiency under the action of AMF	Problems with tuning the NPs size. Fe_3O_4 particles are prone to oxidize into γ-Fe_2O_3 ones	Not employed in this work	
Synthesis in reverse microemulsions	A possibility to synthesize weakly agglomerated crystalline MNPs. Particle size can be controlled through changing surfactants	Problems with a synthesis of a large amount of MNPs. Small particles often display degraded magnetic and heating characteristics	Particle size can be controlled through changing surfactants	Amorphous NPs formed at the initial stage of the synthesis should be subjected to additional heat treatment that results in partial NPs agglomeration. Problems with a synthesis of a large amount of MNPs
Precipitation in nonaqueous solutions	A possibility to synthesize weakly agglomerated crystalline NPs of small sizes	Problems with a synthesis of a large amount of MNPs. Small particles often display degraded magnetic and heating characteristics	–	Amorphous particles formed at the initial stage of the synthesis should be subjected to additional heat treatment that results in partial NP agglomeration. Problems with a synthesis of a large amount of MNPs

Table 1 (continued)

Synthesis method	MNPs with a spinel structural type		MNPs with a perovskite structural type	
	Advantages	Disadvantages	Advantages	Disadvantages
Solgel method	Not employed in this work.		A possibility to synthesize a large amount of MNPs. The formation of the crystalline structure occurs in one stage (without the formation of intermediate phases). At the final stage, the NP agglomeration can be controlled by changing the pH of the medium	Amorphous particles formed at the initial stage of synthesis should be subjected to additional heat treatment that results in the increase of NPs sizes and their partial agglomeration (formation of "bridges" between the particles)

Analysis of the curves showed that the synthesized nanoparticles exhibit behavior close to superparamagnetic [31] and are characterized by weak magnetic hysteresis at both temperatures (see inserts in Fig. 2) and have low coercivity (<2.5 kA/m).

Figure 3 shows plots of magnetic fluid heating temperature (T_{fluid}) versus residence time (τ) in the applied alternating magnetic field. As can be seen, the magnetic fluid based on Fe2 nanoparticles is characterized by a significantly higher rate and temperature of heating than Fe1, Fe3, Fe4, and Fe5 samples. Calculated values of specific loss power (SLP) show that depending on the method of synthesis we can receive nanoparticles characterized by SLP value from 0.2 to 34 W/g. Such behavior of magnetic losses can be related to many factors, particularly to the difference in NPs size (from 6 to 15 nm), variation in magnetic anisotropy energy, etc. [51, 52].

4.2 Spinel Ferrite Nanoparticles with Core/Shell Architecture

Core/shell architecture has acquired increasing interest due to the possibility of combining different materials and fabricating nanostructures with improved characteristics [13, 53]. In addition to varying size, shape, and composition, tuning of magnetic properties through the interface coupling of different magnetic materials becomes a prevailing strategy, introducing a new variable for the rational material design and property control in fundamental science and technological applications [54, 55].

Fig. 2 Hysteresis loops at 300 K and 10 K for Fe_3O_4 nanoparticles synthesized by various methods
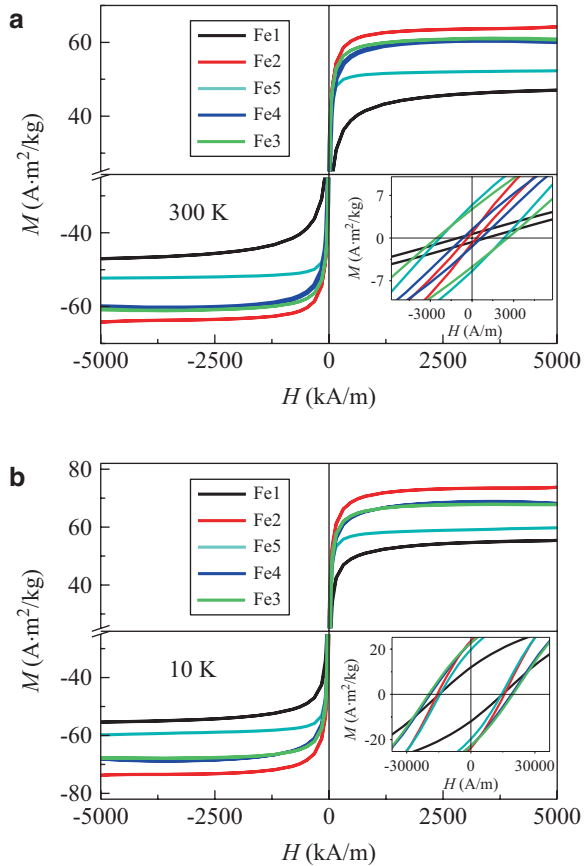
Table 2 The properties of Fe_3O_4 nanoparticles synthesized by various methods

| Sample | d_{TEM}, nm | H_c, A/m | | M_s, Am^2/kg | | T_b, K | SLP, $W/g(Fe_3O_4)$ |
		300 K	10 K	300 K	10 K		
Fe1	6.9±1.9	955	14800	47.0	55.3	92	0.19
Fe2	11.0 ±3.2	318	15760	64.4	74.4	400	33.80
Fe3	11.2±4.1	2550	19660	60.1	67.8	400	25.8
Fe4	15.6±4.8	636	18900	59.8	67.5	400	19.74
Fe5	8.5±3.3	2300	14400	52.2	59.9	400	16.10

Note: d_{TEM} mean size of the nanoparticles obtained from TEM images, *SLP* specific loss power, M_s saturation magnetization, T_b blocking temperature, H_c coercivity

As one of the most important and widely utilized magnetic materials, the spinel ferrite system MFe_2O_4 (M = Fe, Co, Mn, etc.) consists of both magnetically hard and soft materials. For example, cobalt ferrite ($CoFe_2O_4$) is magnetically hard with a large magnetocrystalline anisotropy constant $K > 10^6$ erg/cm^3 [12, 56]. On the

Fig. 3 Dependence of the magnetic fluid temperature versus residence time in the applied AC magnetic field. Magnetic fluids were prepared based on the Fe_3O_4 nanoparticles synthesized by various methods
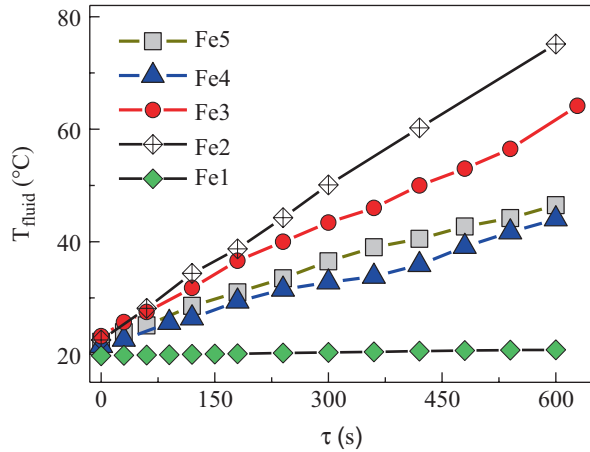
other hand, magnetite (Fe_3O_4) is a ferrite with a much smaller magnetic anisotropy constant $K \sim (10^4 \div 10^5)$ erg/cm^3 [57, 58]. Due to the same crystallographic structure and almost negligible lattice mismatch among these spinel ferrites, it should be markedly controllable to epitaxially grow a uniformed shell over a core. Among other things, such kind of the well-defined bimagnetic spinel ferrite nanocrystals with core/shell architecture can provide a better platform for the fundamental understanding of magnetism and the relationship between crystalline structure, morphology, and physical properties.

In works [14, 59, 60], the effect of shell thickness on DC magnetic parameters (saturation magnetization, coercivity, blocking temperature) and AC losses (specific loss power, intrinsic loss power) has been studied for Fe_3O_4/$CoFe_2O_4$ core-/shell-like magnetic nanoparticles with a fixed diameter of core ~6.3 nm and an effective thickness of shell up to 2.5 nm. Also, the comparison of the properties of Fe_3O_4/$CoFe_2O_4$ core/shell nanoparticles and the mechanical mixture of the Fe_3O_4 and $CoFe_2O_4$ nanoparticles taken in appropriate proportions was done, which emphasized the role of interface phenomena at the Fe_3O_4–$CoFe_2O_4$ boundary in the formation of magnetic properties core/shell nanoparticles and discussed the way to tune and optimize the parameters of compositional nanoparticles for their use in various technological and biomedical applications.

The synthesis of core/shell structures has remained a complex approach, since it should enable a high crystalline quality of both core and shell, guarantee their good epitaxy, and minimize intermixing processes at the core–shell interface. For this reason, the results of earlier works carried out in our and other groups were taken into account while fabricating Fe_3O_4/$CoFe_2O_4$ core-/shell-like nanoparticles [31, 59, 61–63]. In our previous works, the combination of X-ray diffraction and ^{57}Fe Mössbauer spectroscopy studies made it possible to conclude that among several MNPs synthesis methods, only the method of coprecipitation from diethylene glycol (DEG) solutions allowed fabrication of magnetite MNPs with the smallest amount of maghemite and goethite phases [31, 59]. Therefore, it is the method of

coprecipitation from DEG solutions that was chosen to fabricate the nanoparticles in the present work.

Broad studies were carried out to make sure that synthesized nanoparticles have the core/shell architecture and are not the mechanical mixture of Fe_3O_4 and $CoFe_2O_4$. Considering that individual Fe_3O_4 and $CoFe_2O_4$ MNPs have the same crystalline structure with close lattice parameters, the shell cannot be reliably distinguished from the core by the contrast of the TEM image. Therefore, before this work, a number of special experiments were carried out to check if the composite Fe_3O_4/$CoFe_2O_4$ MNPs have a core-/shell-like structure [31, 59]. The experiments included a comparative analysis of the most intensive (311) XRD peak collected from separate Fe_3O_4 and $CoFe_2O_4$ MNPs, a mechanical mixture composed of these compounds, and composite Fe_3O_4/$CoFe_2O_4$ particles. Besides, corresponding TEM and ^{57}Fe Mössbauer investigations were carried out on the individual and composite MNPs. As described in detail in Ref. [60], the results confirmed the formation of a core/shell-like structure rather than a mechanical mixture. At the same time, as follows from Refs. [59, 61, 63], the particles may contain quite a noticeable transitional layer between the core and the shell, which may be composed of $Co_{1-x}Fe_{2+x}O_4$ phases with a gradient of Co concentration from the surface to the core.

Results of XRD study of the synthesized nanostructures were analyzed in detail in Ref. [14]. All synthesized samples have a cubic spinel structure (JCPDS 19-0629) with no traces of impurity.

As can be estimated from the results of TEM investigations, the size of the Fe_3O_4 NPs is ~ 6.3 nm and grows with the increase of effective thickness (t_{shell}) of the $CoFe_2O_4$ shell according to the calculations (Fig. 4).

Studies of field and temperature dependences of the magnetization of Fe_3O_4/$CoFe_2O_4$ core/shell nanoparticles with different shell thicknesses have shown that the addition of the shell leads to a sharp increase in coercive force as well as in the blocking temperature [14, 60]. Effective anisotropy constants K_{eff} were calculated based on a simple approach of coexisting superparamagnetic and blocked magnetic nanoparticles [12, 13, 64]. It was shown that shell addition and subsequent increase
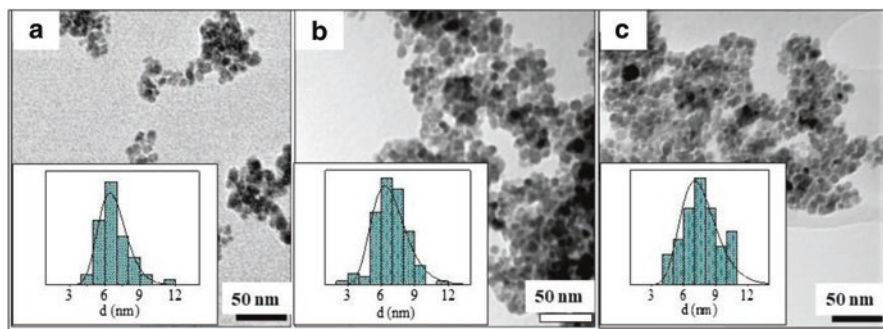
Fig. 4 TEM images of Fe_3O_4/$CoFe_2O_4$ nanoparticles with $tCoFe_2O_4 = 0$ nm (**a**); 0.05 nm (**b**); and 1 nm (**c**). Insets show the diagrams of size distribution for corresponding ensembles of nanoparticles (the units of abscissa axes are nanometers)

in its thickness lead to the strong increase of K_{eff} with a simultaneous decrease in magnetization. It is noteworthy that qualitatively similar behavior was observed in $MnFe_2O_4/CoFe_2O_4$ and $ZnFe_2O_4/CoFe_2O_4$ core/shell nanoparticles [60].

To obtain the AC magnetic heating characteristics of the synthesized MNPs, the time dependence of heat generation was studied under AMF with fixed amplitude $H_{max} = 100$ Oe and frequency $f = 300$ kHz [18, 65]. The plots of magnetic fluid temperature (T_{fluid}) versus heating time in external AMF (τ) for the fluids based on synthesized MNPs are shown in Fig. 5. Based on these data, the values of SLP were determined and compared with those calculated from the area of magnetic hysteresis loops. Figure 6 compares both sets of SLP vs t_{shell} dependences. Open squares show the data determined from experimental T_{fluid} vs t dependences. Filled triangles mark SLP values calculated as

$$SLP = \mu_0 f A_{loop} / \rho, \tag{1}$$

where $\mu_0 = 4\pi\ 10^{-7}$ H/m and ρ is the MNPs material mass density [18, 66]. It is seen that general trends in both sets of SLP vs t_{shell} dependences comply with each other. The discrepancies observed between experimental and calculated SLP values can originate from a nonnegligible effect of frequency change on coercivity and hysteresis loop shape [12, 13, 64].

As seen in Fig. 6, the addition of 1.0 nm $CoFe_2O_4$ shell to the Fe_3O_4 core strongly enhances the heating efficiency of the obtained composite MNPs. Thus, core/shell-like architecture can serve as an efficient tool to govern both the DC and AC behavior of magnetic nanoparticles.

Magnetic and calorimetric properties of the core/shell nanoparticles based on other spinel ferrites ($MnFe_2O_4/CoFe_2O_4$, $ZnFe_2O_4/CoFe_2O_4$, etc.) also were studied by our and other research groups [67–69]. The results show that the addition of the shell has a significant impact on the saturation magnetization, effective anisotropy
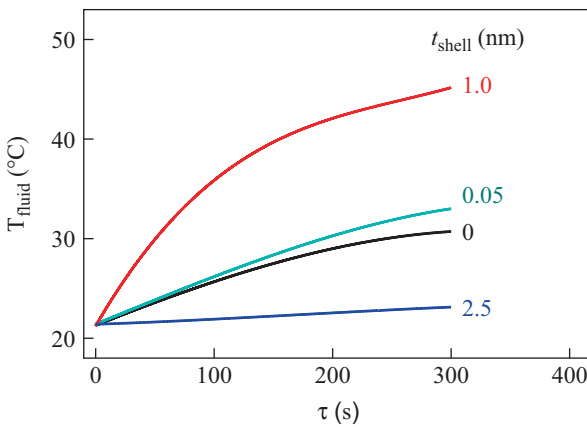
Fig. 5 Fluid temperature T_{fluid} versus heating time τ dependences for magnetic fluids based on Fe/Co(t_{shell}) MNPs

Fig. 6 Experimentally determined (open squares) and calculated (filled triangles) SLP values as functions of shell thickness for Fe/Co(t_{shell}) MNPs
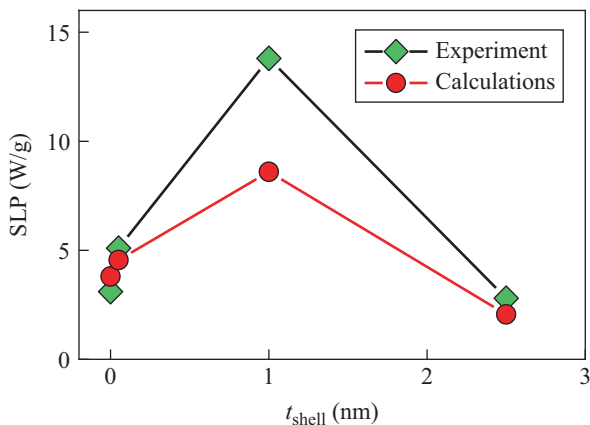
constants, temperature behavior of compositional nanoparticles, and their efficiency of heating in the applied AC magnetic field.

Major trends in the heating abilities as a function of the core size, the nature, and the thickness of the shell were outlined in Ref. [70] based on the systematic fundamental study of $CoFe_2O_4/MnFe_2O_4$ and $CoFe_2O_4$/spinel iron oxide core–shell MNPs confirmed by experiments conducted on the water-based ferrofluids. At the same time, the authors stress that all the findings seem to depict a more complex scenario behind the heating abilities of bimagnetic core–shell systems than simple relationships with single magnetic or microstructural parameter(s). It follows from all the available data that the coating of MNPs with the shells leads to the transformation of the parameters of both the *initial nanoparticle* and *its shell* and, as a result, it makes the particles acquire *new characteristics that are typical neither for the core nor for the shell.*

Obtained results pave the way to tune and optimize open the parameters of spinel ferrite nanoparticles with core/shell-like architecture for their use in various technological and biomedical applications.

5   Materials with Automatic Preset Temperature Control when Used in MHT

5.1   *Nickel–Zinc Spinel Nanoparticles: Magnetic Characterization and Prospects of the Use in Self-Controlled Magnetic Hyperthermia*

It was noted above that for the use of materials in self-controlled MHT, the Curie temperature of these materials must be slightly above the therapeutic range of hyperthermia. One of the effective methods for controlling the Curie temperature in

ferrite spinel materials is the use of solid solutions. In [15], the effectiveness of this approach was demonstrated using nickel–zinc spinels as an example.

Bulk $NiFe_2O_4$ is a soft ferrimagnet with mass magnetization ∼56 A·m^2/kg and Curie temperature $T_C \approx 658$ K [67, 71]. On the contrary, bulk $ZnFe_2O_4$ is an antiferromagnet with a Neel temperature of ∼9.5 K [16, 67]. Heavily Zn-substituted ($x > 0.5$) bulk samples of $Ni_{1-x}Zn_xFe_2O_4$ display reduced values of saturation magnetization and Curie temperature [4, 15]. Although the properties of these ferrites can be strongly altered at the nanoscale, it is expected that Zn substitution for Ni will make it possible to preset the Curie temperature slightly above the hyperthermia therapeutic range to reach the self-controlled heating regime.

The important issues were: (1) to find the regularities of the effect of zinc substitution on magnetic parameters and heating characteristics of nickel–zinc spinel nanoparticles; (2) determine the concentration region where Curie temperature is close to the range of hyperthermia therapy (∼330 K); (3) experimentally verify the idea of controllability of the MNP thermal response to the action of AC magnetic field; (4) weigh up the prospects of the use of synthesized MNPs in self-controlled magnetic nanohyperthermia.

Nanopowders of $Ni_{1-x}Zn_xFe_2O_4$ ($x = 0 - 1$) with mean grain size of ∼50 nm (see inset in Fig. 7) were synthesized via a method of hydroxide precipitation. Details of the samples preparation are described in Refs. [72, 73]

Figure 7 presents concentration dependences of spontaneous magnetization at 140 K and 300 K. Nonmonotonous character of $M_s(x)$ dependences implies that the substitution process is accompanied by the processes of redistribution of cation ions between different sites of spinel structure [73]

Bulk $NiFe_2O_4$ is a well-known inverse spinel with Ni^{2+} ions on B sites and Fe^{3+} ions distributed equally among A and B sites, where A and B indicate tetrahedral and octahedral sites of the spinel structure, respectively [74]. Morr and Haneda have
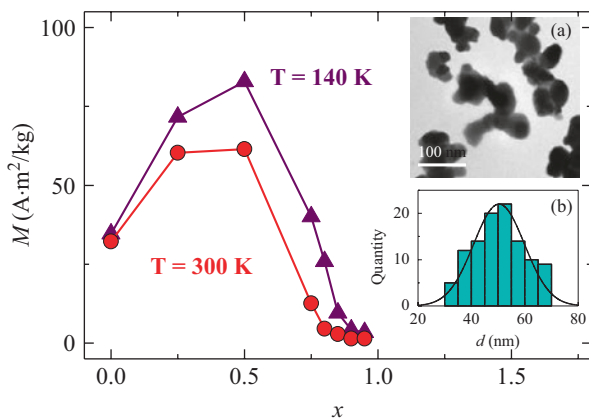
Fig. 7 Dependences of mass magnetization on zinc content for $Ni_{1-x}Zn_xFe_2O_4$ nanoparticles. Inset shows (**a**) a fragment of a microphotograph of $Ni_{0.25}Zn_{0.75}Fe_2O_4$ MNPs and (**b**) the diagram of MNPs size distribution

shown that $NiFe_2O_4$ in the ultrafine form exhibits noncollinear spin structure and that the magnetic moment at low temperatures is appreciably lower than the value for the bulk material [67]. They have proposed a model wherein the particle consists of a core with the collinear spin arrangement and a surface layer with the magnetic moment inclined to the direction of core magnetization. Our results agree with this picture: M_s of $NiFe_2O_4$ MNPs (~35 A·m²/kg) is by far smaller than that of the bulk sample (~56 A·m²/kg).

Bulk $ZnFe_2O_4$ has a normal spinel structure, in which all Zn^{2+} ions occupy tetra-hedral positions (A sites) and all Fe^{3+} ions—octahedral positions (B sites). Zinc ferrite is paramagnetic at room temperature, and the transition to a magnetically ordered (antiferromagnetic) state occurs only at temperatures of about 9.5 K [67, 75]. The magnetic properties change significantly when the particle size decreases to a few tens of nanometers: At this scale, a cation inversion occurs; i.e., a part of zinc ions occupy the B sites and part of iron ions—the A sites [16, 75, 76]. Thus, there is a transformation of structure from normal to mixed spinel which disturbs a balance in the system of competing magnetic interactions and, as a rule, leads to the appearance of resultant spontaneous magnetization. The degree of cation inversion depends on several factors, including the particle size [53]. The contribution from the subsurface region which is usually characterized by a noncollinear magnetic ordering depends on the particle size as well [72, 75].

As seen from Fig. 7, the substitution of Zn for Ni results in an initial rise of spon-taneous magnetization followed by a rapid decrease as x exceeds 0.75. As x crosses 0.85, the spontaneous magnetization levels off at $M_s \approx 2$ A·m²/kg. Similar trends were observed in works [77] and ascribed to the incomplete ordering of Ni^{2+} and Fe^{3+} ions between the octahedral and tetrahedral sites in the spinel.

To obtain the AC magnetic heating characteristics of the synthesized MNPs, the time dependence of heat generation was studied under AMF with fixed amplitude $\mu_0 H_{max}$=10 mT and frequency f=300 kHz.

The plots of magnetic fluid temperature versus residence time in external AMF for the fluids based on synthesized MNPs are shown in Fig. 8. For the samples with

Fig. 8 Fluid temperature T_{fluid} versus heating time τ dependences for magnetic fluids based on $Ni_{1-x}Zn_xFe_2O_4$ nanoparticles. The temperature region, which is suitable for hyperthermia treatment, is hatched. Inset shows concentration dependences of Curie temperature (T_C) and maximal temperature of the sample heating under the action of AMF (T_s)
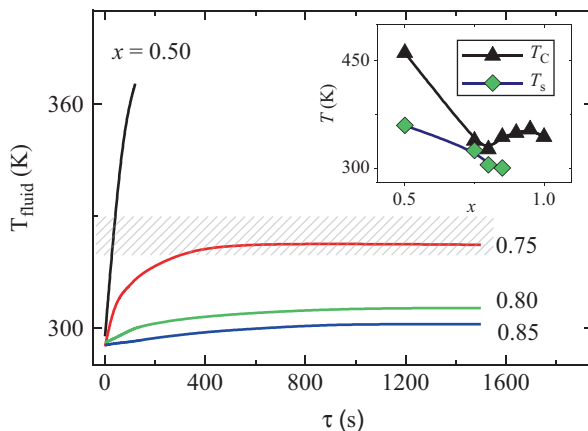
$x \le 0.5$, T_{fluid} rapidly grows and in less than 1 min approaches the temperature of fluid boiling. This makes it impossible for an accurate determination of the temperature at which T_{fluid} achieves saturation. What is more, as follows from the data of work [19, 78–85], the precision of calorimetric measurements gets worsened in the vicinity of the fluid boiling point and the results of measurements become unreliable. For this reason, further analysis will mainly be focused on the samples with a higher zinc content ($x > 0.5$), and in some cases, the data for the sample with $x=0.5$ will be presented for reference.

It is important that after an abrupt initial temperature rise, the $T_{fluid}(\tau)$ curves reach saturation at a certain T_s value. Inset of Fig. 8 compares the values of T_s and Curie temperature T_C of the nanoparticles. It is observed that these values are quite close for the samples with x near 0.75, although for other samples there is a noticeable difference between T_s and T_C (for the rest of the samples, the difference exceeds a few tens of Kelvins).

The observed discrepancy between T_s and T_C for the samples with $x > 0.8$ can be easily understood since these samples display negligible heating efficiency which is not enough to appropriately heat the samples. Among other factors affecting a degree of proximity of T_s to T_C, it should noted that T_s is sensitive to the features of heat exchange with the environment, magnetization value, dispersion of magnetic parameters, etc.

The hatched region in Fig. 8 shows the temperature range which is suitable for hyperthermia therapy. It is seen that MNPs with $x \approx 0.75$ display T_s value within this region, and thus, *they are promising heat mediators for self-controlled magnetic nanohyperthermia*.

5.2 *(La, Sr)MnO₃ Nanoparticles as Promising Heat Mediators for Self-Controlled Magnetic Hyperthermia*

The idea of using manganite nanoparticles to implement self-controlled MHT was first proposed in 2002 [86], but research in this direction was intensified only after the publication of experimental results by a group of Czech and French scientists led by E. Pollert in 2006 [87]. Today, there is an active scientific work on the study and optimization of the properties of these materials (see, for example, [21, 48, 81, 88–90]).

Magnetic state of $La_{1-x}Sr_xMnO_3$ manganite strongly depends on strontium content x [78, 79]. Bulk samples with Sr concentration $0.15 \le x \le 0.60$ are ferromagnetic [38, 39, 48]. The Curie temperature T_C displays a maximum at $x = 0.33$ ($T_{Cmax} = 370$ K) and is quite sharply reduced as x deviates from 0.3. Since the development of heat mediators for self-controlled MHT requires NPs with T_C close to 320 K, in this work $La_{1-x}Sr_xMnO_3$ nanoparticles with a chemical composition of $x = 0.22$ were studied.

A study of the properties of LSMO MNPs synthesized by deposition from DEG, deposition from the reverse microemulsions and the solgel method [39] showed that the amorphous nonmagnetic precursor is formed immediately after synthesis in all three methods. A single-phase crystalline structure begins to form in one stage at a temperature of 600 °C and is completely formed at 800 °C. Manganite nanoparticles synthesized by three different methods have average sizes of 20–40 nm with a narrow size distribution [18].

In this work, the deposition from the reverse microemulsions was used for synthesizing LSMO MNPs. X-ray diffraction studies confirmed the single-phase structure of the samples [88, 89, 91, 92], and TEM measurements showed that the average size of nanoparticles is about 30 nm (see inserts in Fig. 9).

Figure 9 shows the temperature dependences of mass magnetizations M_{fc} and M_{zfc}, obtained in the magnetic field $\mu_0 H = 2$ mT. The $M_{fc}(T)$ and $M_{zfc}(T)$ curves coincide at temperatures higher than 320 K but diverge in the low-temperature region. $M_{fc}(T)$ is a declining function of temperature, while $M_{zfc}(T)$ is a curve with a maximum. The quasistatic (i.e., low frequency, with $10^{-4} < f < 10^{-2}$ c^{-1}) blocking temperature defined as a temperature at which $M_{zfc}(T)$ achieves a maximum is $T_b = 285$ K.

In Fig. 10, hysteresis loops $M(H)$ obtained at $T = 295$ K and 10 K are presented. Both curves have a tendency to saturation in strong fields ($\mu_0 H > 300$ mT). The values of saturation magnetization, defined as magnetization in a field of 1 T, are as follows: $M_s|_{T=10K} \approx 81$ A·m^2/kg and $M_s|_{T=295K} \approx 47$ A·m^2/kg. The M vs. H curves are characterized by coercivities $\mu_0 H_c \approx 22.7$ and 1.2 mT at $T = 10$ K and 295 K, respectively (see inset of Fig. 10).

To obtain the AC magnetic heating characteristics of the synthesized LSMO MNPs, the time dependence of heat generation was studied under AMF with a fixed amplitude H_{amp}, varying in the range from 5.6 to 10.5 mT in different experiments, and frequency $f = 300$ kHz. The plots of magnetic fluid temperature versus residence time in an AMF, $T_{fluid}(\tau)$, for the fluids based on the synthesized LSMO MNPs

Fig. 9 Temperature dependences of mass magnetizations M_{fc} and M_{zfc} for LSMO MNPs. The inset shows (**a**) the microphotograph of LSMO MNPs and (**b**) their size distribution diagram
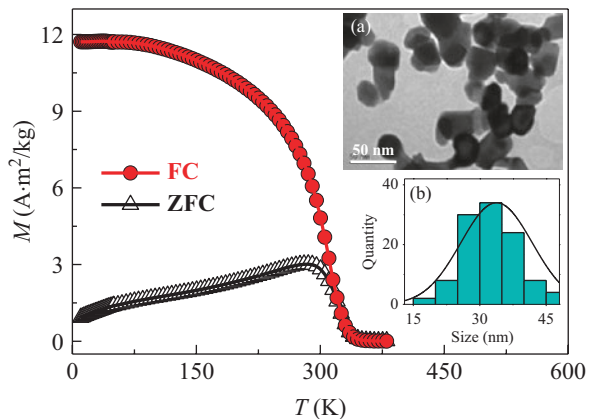
Fig. 10 Magnetization
loops $M(H)$ at $T = 295$
K and 10 K. The inset
shows the same
dependences in the region
of weak fields
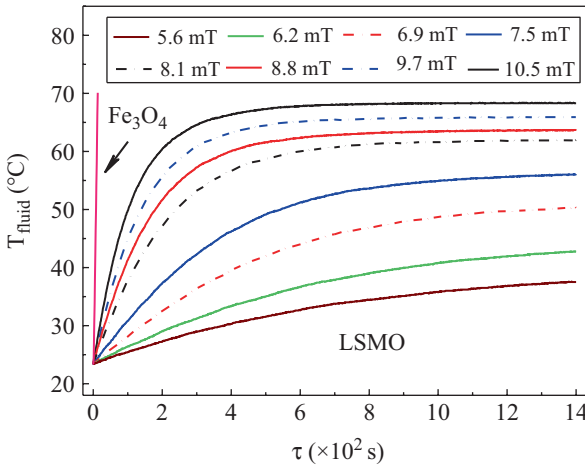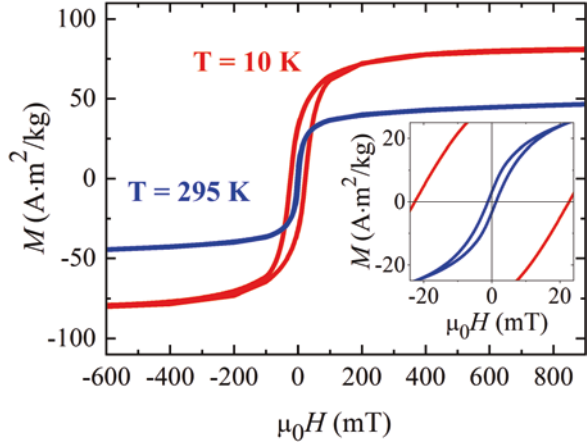
Fig. 11 Time dependences of the fluid temperature $T_{fluid}(\tau)$ for the fluids based on LSMO MNPs
in an AMF with different amplitude values: $\mu_0 H_{amp} = 5.6$; 6.2; 6.9; 7.5; 8.1; 8.8; 9.7; 10.5 mT and
frequency $f = 300$ kHz. For comparison, the $T_{fluid}(\tau)$ dependence is shown for the fluid based on
Fe_3O_4 MNPs in an AMF with the same frequency and $\mu_0 H_{amp} = 10.5$ mT

are shown in Fig. 11. Magnetic fluid warms up due to the magnetic losses in AMF
$H(t) = H_{amp} \cos (2\pi ft)$.

In experimental measurements, the initial temperature of magnetic fluid before
applying the AC magnetic field was 23.5 °C. It is seen from the curves of Fig. 12
that after a sharp initial rise, the change of T_{fluid} with τ becomes slower and
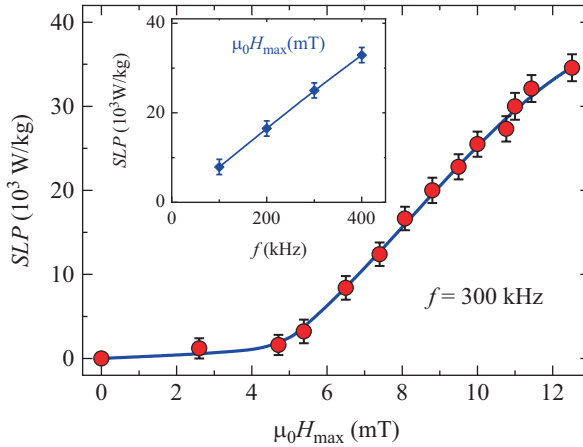
Fig. 12 SLP vs. H_{max} dependence measured at $f = 300$ kHz. The inset shows SLP vs. f dependence obtained at $\mu_0 H_{max} = 10$ mT

eventually these dependences tend to saturate. For comparison, the $T_{fluid}(\tau)$ dependence is added for the fluid based on Fe_3O_4 MNPs (~12 nm in size) subjected to the AMF with the same frequency and $H_{amp} = 10.5$ mT. The temperature of the Fe_3O_4 MNP-based fluid rapidly grows and immediately approaches the temperature of boiling.

With the increase in H_{amp}, the saturation temperature T_s rises, but eventually, it approaches the Curie temperature of the LSMO nanopowder $T_C \sim 70$ °C [9, 93–96]. This means that the idea of self-controlled heating where the heating efficiency sharply reduces as the fluid temperature approaches T_C of LSMO MNPs is valid. It should be noted that relatively small values of H_{amp} (< 10.5 mT) are not enough to warm up the magnetic fluid to the T_C of LSMO nanopowder, and in these cases, the thermal equilibrium occurs at lower temperatures, i.e., at T_s being lower than 70 °C.

The initial slope of each curve plotted in Fig. 12 provides information about specific loss power [97, 98]. The SLP values, which depend on the parameters of the applied AC field, were calculated for a range of magnetic field amplitudes $\mu_0 H_{max}$ and frequencies f. The details of the SLP calculation are described in Refs. [93, 99, 100].

Figure 12 shows SLP vs. H_{max} dependence obtained at $f = 300$ kHz. SLP is negligibly small at weak magnetic fields ($\mu_0 H_{max} < 5$ mT), rapidly rises in the region from ~5 to ~10 mT, and then displays a tendency to saturation. In the region from 6 to 9 mT, the SLP(H_{max}) dependence is almost linear.

It was reported in Refs. [20, 93, 97, 101] that the obtained value is high enough for the use of the MNPs as HT heating mediators in the treatment of cancer diseases. The mechanisms responsible for high heating efficiency of LSMO MNPs will be discussed below.

6 Mechanisms of Losses in Magnetic Nanoparticles and Fluids Based on Them

6.1 General Description of the Energy Loss Mechanisms

If a magnetic fluid based on single-domain ferromagnetic nanoparticles is subjected to AMF action, a part of the field energy is dissipated by the nanoparticles and transformed into heat. For magnetic HT, low-concentrated suspensions of MNPs in dielectric fluids are usually used [100]. In this case, interparticle interaction is assumed to be negligible and the energy dissipation can be described as a sum of processes occurring in separate particles.

The array of MNPs can dissipate the energy of the AMF into the environment due to the processes of remagnetization of nanoparticles or due to the rotation of the nanoparticle as a whole. The last-mentioned process is called Brown relaxation (BR losses). Remagnetization losses depend on the relationship between the characteristic parameters of MNP (saturation magnetization M_s, the effective magnetic anisotropy constant K_{eff}, the coercive force H_C, the volume of the MNP V and the relaxation time of the MNPs system τ and external parameters, the frequency f of the external magnetic field, as well as the temperature T) and require separate consideration.

1. **BR losses**. In fluid suspensions, the relatively high anisotropy barrier may be overcome by rotation of the whole particle under the influence of the AMF. In this case, frictional losses due to viscosity η of the carrier liquid arise. The resulting relaxation time is given by [99, 100, 102]

$$\tau_B = \frac{4\pi\eta R_h^3}{k_B T},$$ (2)

where R_h is the hydrodynamically effective radius, which may differ from the geometrical one [103]. The specific losses power caused by this mechanism is calculated by the formula (3) provided below.

2. **Remagnetization losses.** The behavior of single-domain MNPs depends on the energy balance between anisotropy ($\varepsilon_a = K_{eff} \cdot V$) and thermal fluctuation ($\varepsilon_T \approx k_B \cdot T$) contributions (here, k_B is the Boltzmann constant). In the limit $\varepsilon_T \gg \varepsilon_a$, the magnetic moment of a particle can be considered as freely fluctuating. This results in the phenomenon of superparamagnetism, where the ensemble of particles behaves like a paramagnet consisting of particles with very large magnetic moments. In the opposite limit, when $\varepsilon_T \ll \varepsilon_a$, the particle magnetic moment is blocked on a time scale given by the experiment and lies parallel or antiparallel to the easy magnetization axis. The transition to the latter state occurs at the so-called blocking temperature T_b, below which the particle moments appear frozen on the time scale of the measurement τ_m. The T_b value depends on the measurement duration and can be determined from the temperature dependences of magnetization: The zero-field-cooled (ZFC) magnetization M_{zfc} measured in a weak magnetic field achieves a maximum at T_b [66]. The ZFC magnetization curve is

usually measured in quasistatic measurements with increasing temperature in a weak magnetic field after cooling the specimen in the absence of a magnetic field down to $T \ll T_b$. The measurement duration in such a case is of the order of hundreds of seconds.

For two cases, particularly, when the nanoparticle is (1) in the superparamagnetic state or (2) in the blocked state, analytical approaches have been developed to estimate the energy losses due to remagnetization. To describe energy losses in the first case (superparamagnetic behavior), we talk about Neel relaxation (NR losses: also called Neel–Arrhenius or Neel–Brown relaxation). In the second case (blocked state), the term hysteresis losses or remagnetization based on the Stoner–Wohlfarth model (SW losses) is used [9]. In the region of transition from the equilibrium superparamagnetic to the blocked state, only numerical simulation is correct [66, 98, 100, 101, 104].

2.1. NR losses. If thermally activated fluctuations of the magnetic moment direction are fast compared to the measurement duration ($\tau < \tau_m$), the behavior of the ensemble of MNPs can be described by a linear response theory (LRT) with relaxation time taken in Neel–Brown form [18]. In this case, specific power dissipated by an ensemble of MNPs is described by [9]:

$$P_{NR} = f \mu_0 \int_0^{1/f} \tilde{M} dH = f \pi \mu_0 \chi'' H_{max}{}^2 = \frac{2\mu_0 \pi^2 f^2 \tau}{1 + (2\pi f \tau)^2} \chi_0 H_{max}{}^2. \tag{3}$$

It is seen that P_{NR} displays a quadratic dependence on AMF amplitude H_{max}. As a function of frequency, it is quadratic at low values of f ($2\pi f \tau \ll 1$), deviates from quadratic law as f increases, and tends to saturation at high frequencies ($2\pi f \tau \gg 1$), where the saturated value reads:

$$P_{NR}^{f \to \infty} = \frac{\mu_0 \chi_0 H_{max}{}^2}{2\tau}. \tag{4}$$

Heating efficiency under such conditions ($2\pi f \tau \gg 1$) does not depend on frequency.

In a general case, both the Brown relaxation process and the Neel relaxation process may be present, but the faster one is dominant.

2.2. SW losses. If thermally activated fluctuations of the magnetic moment direction are not fast in comparison with the measurement duration ($\tau > \tau_m$), the system is in the blocked state and the dependence of power losses on the magnetic field is of threshold character.

For the case of weak magnetic fields ($H_{max} \ll H_a$), the reaction of the system to the external magnetic field will be very weak, remagnetization practically would not occur (only a minor hysteresis loop will be observed), and, thus, the power of dissipation will be negligible. If the amplitude of the magnetic field equals or exceeds the anisotropy field, the shape and area of the hysteresis loop will approach, but would not exceed a theoretical limit which is described by the Stoner–Wohlfarth model [66, 104].

If an ensemble of MNPs is put into an AMF, the amount of heat dissipated in MNPs during one cycle of the magnetic field is equal to the area of hysteresis loop S. The dissipated energy per second per unit volume of MNPs is then given by:

$$P_{\text{SW}} = Sf. \tag{5}$$

For the MNP in a blocked state and with its easy axis aligned along the magnetic field direction, the hysteresis loop is a rectangle with temperature-dependent H_C. At low temperatures ($T \rightarrow 0$), the temperature-activated repopulation of energy minima is suppressed, and remagnetization can only occur when the energy barrier is fully removed by the magnetic field. This occurs when H_{max} reaches anisotropy field H_a [18]. Thus, for the Stoner–Wohlfarth model $H_c \rightarrow H_a$ as $T \rightarrow 0$. For an optimal case where $H_{\text{max}} = H_c$:

$$P_{\text{SW}} = 4\mu_0 H_{\text{max}} M_s f. \tag{6}$$

To estimate P_{SW} in all other cases, it is convenient to use the formula:

$$P_{\text{SW}} = 4\alpha\mu_0 H_{\text{max}} M_s f, \tag{7}$$

where α is a dimensionless parameter which equals the ratio between the areas of actual hysteresis loop and ideal rectangle loop, with the latter having $\alpha = 1$. For the ensemble of MNPs with randomly oriented anisotropy axes and optimally chosen relation between H_c and H_{max} ($H_c = 0.81 H_{\text{max}}$), $\alpha = 0.39$ [66, 104]. When H_{max} is less than a field at which magnetization saturation occurs, α is a function of H_{max}.

As a result, the upper limit of P_{SW} for the ensemble of MNPs with randomly oriented anisotropy axes is:

$$P_{\text{SW}}^{\text{limit}} = 4 \cdot \alpha \cdot \mu_0 H_{\text{max}} M_s f \mid_{\alpha=0.39}. \tag{8}$$

The values of α observed in the experiment do not exceed 0.3 [20, 71, 80, 98, 104].

6.2 Low- and High-Frequency Measurements

A usual way to model remagnetization processes and calculate SLP values is to use the MNP parameters extracted from LF measurements [18]. It should be noted, however, that such parameters as blocking temperature T_b and coercivity H_c are frequency dependent. This means that not only SLP values calculated with the use of magnetostatic parameters could be incorrect, but also the mechanisms of AC losses could become different as measurement conditions change from magnetostatic to HF (~100 kHz) ones.

It was noted above that blocking temperature T_b is the temperature at which a condition [18]

$$\tau_m = \tau \Big|_{T=T_b}. \tag{9}$$

is satisfied. At this temperature, the rate of thermally activated processes becomes insufficient to get the system into equilibrium, and MNP magnetic moment remains blocked in a metastable state.

Formula (9) makes it possible to estimate the dependence of blocking temperature on measurement time. Assuming that a time scale of measurements is $1/f$, T_b can be roughly estimated as

$$T_b \approx K_{\text{eff}} V / \left(k_B \ln\left(\frac{1}{f\tau_0} \right) \right). \tag{10}$$

If MNP magnetic parameters, in particular K_{eff}, were temperature independent, the change in the AMF frequency from ~0.01 Hz (magnetostatic measurements) to ~10^5 Hz (the frequencies at which usually HT treatment is carried out) would result in the increase of T_b by (2–3) times. Thus, for the case where the T_b^{hf} value exceeds ~150 K, the T_b^{lf} value can exceed room temperature. This means that the mechanism responsible for AC losses in the vicinity of room temperature will be SW mechanism, rather than NR one, as follows from LF measurements.

Figure 13 illustrates $M_{zfc}^{lf}(T)$ and $M_{zfc}^{hf}(T)$ dependences obtained from LF and HF measurements, respectively. For each of these curves, magnetization reaches a maximum at temperature which equals the blocking temperature. Since $T_b^{lf} \ll T_b^{hf}$, the temperature region within which SW mechanism is responsible for the losses is by far wider in the latter case (HF measurements) than in the former one (LF measurements).

The scheme in Fig. 13 is given under the assumption that $T_b^{hf} \ll T_C$. For the case, where T_b^{hf} is close to T_C, the relation between T_b^{lf} and T_b^{hf} will qualitatively be the same, but quantitative difference between them will change. Naturally, T_b cannot exceed T_C.

Thus, approaches based on modeling of remagnetization processes at high frequencies (~ 100 kHz) using magnetic parameters of MNPs obtained from magnetostatic measurements are not always correct. Because the blocking temperature and coercive force depend on the frequency, the high-frequency remagnetization processes can be qualitatively different from the low-frequency ones.

6.3   Energy Losses in (La, Sr)MnO₃ Nanoparticles

As was mentioned above, the approaches based on the use of quasistatic measurement results are not always correct for describing processes occurring in alternating fields with frequencies used in MHT (~ 100 kHz). Let's consider the situation on the example of the properties of the LSMO MNPs described in the previous section.
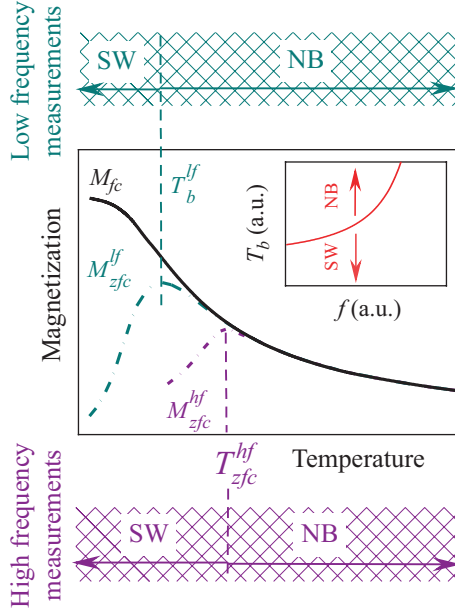
Fig. 13 Illustration of the behavior of magnetization resulted from LF and HF measurements. The inset presents the frequency dependence of blocking temperature T_b. M_{fc}—field-cooled magnetization, M_{zfc}^{lf} and M_{zfc}^{hf}—the zero-field-cooled magnetization values resulted from LF and HF measurements, respectively. T_b^{lf} and T_b^{hf}—the values of blocking temperatures resulted from LF and HF measurements, respectively. Top and bottom diagrams schematically illustrate temperature regions, where either SW or NR mechanism of losses dominates for LF and HF cases, respectively

As seen in Fig. 9, the blocking temperature of the LSMO MNPs is lower than room temperature, so in the range of room temperature and above, it should be expected that the NR mechanism is dominant. But the data in Fig. 12 suggest another. First, the dependence of SLP on AMF amplitude is of threshold character: SLP becomes noticeable only when H_{max} exceeds a certain value. Second, the SLP is almost a linear function of AMF frequency (see the inset of Fig. 12). Such kinds of SLP(H_{max}) and SLP(f) dependences are characteristic only for SW losses. As follows from formulae (2), (3) and (4), NR and BR losses display quadratic dependence on AMF amplitude. What concerns frequency dependence of SLP, NR and BR losses either display quadratic SLP(f) dependence or are frequency independent. Thus, the character of SLP(H_{max}) and SLP(f) dependences indicates that SW mechanism is responsible for LSMO MNPs heating.

The calculations performed in [21, 105–107] show that for the LSMO MNPs under investigation only SW mechanism can provide sufficiently high energy losses which correspond to experimentally obtained value of SLP ($\mu_0 H_{max} = 10$ mT) $\approx 25 \times 10^3$ W/kg; the other kinds of AC losses are so weak that they cannot be responsible for LSMO MNP heating. It also follows from the calculations that SLP can be increased by about an order of magnitude by means of optimization of the

parameters of LSMO MNPs (weakening agglomeration, narrowing size distribution, and attaining uniformity of geometrical and magnetic parameters) and corresponding adjustment of AMF parameters.

The obtained data indicate the directions of further optimization of nanoparticle parameters for use in MHT [39].

7 Biomedical Investigations

It was mentioned above that NPs of lanthanum–strontium manganite are promising for application in self-controlled magnetic HT. However, the issues concerning their toxicity and biocompatibility have been investigated only episodically to this time [6, 107].

7.1 Development of Magnetic Fluids

To investigate the biomedical features of magnetic LSMO NPs as the heat mediators for magnetic hyperthermia, it is necessary to develop the magnetic fluid for the possibility to inject such NPs into the tumor. Magnetic fluid (MF) is the suspension of nanosized ferromagnetic or ferrimagnetic particles, stabilized in the polar or nonpolar medium using surfactants or polymers.

To perform the biomedical investigations of manganite NPs, particles synthesized via the solgel method (NPs synthesized in such way had one of the highest SLP values [108]) were dispersed in 0.1% aqueous agarose solution by ultrasound for obtaining the magnetic fluid with the concentration of magnetic phase of 50 mg/ml [109].

7.2 Performing the Biomedical Investigations of Magnetic Fluid Based on Manganite NPs *in vitro and* in vivo

At present, it is known about the active investigations of Fe_3O_4 NPs in medicine due to their biocompatibility [22]. Therefore, to estimate the prospects of LSMO NPs in this area, it is important to investigate their biomedical characteristics and compare them with known Fe_3O_4 NPs. The first stage of biomedical investigations of magnetic fluid based on the synthesized LSMO NPs included a number of *in vitro* investigations [110].

Comparison of magnetic fluids based on Fe_3O_4 and LSMO NPs was performed on the ST and MCF-7S cell lines using four characteristics: *cytotoxicity,*

Table 3 Comparison of cytological properties of Fe_3O_4 and LSMO NPs

Characteristic	Fe_3O_4	LSMO
Cytotoxicity	Maximum permissible concentration	
	1.1 mg/ml	5 mg/ml
Genotoxicity	Possess a small genotoxic effect in the concentration of 0.9 mg/ml	Does not possess any genotoxic effect
Antioxidant activity	Does not display antioxidant activity	Displays antioxidant activity in the concentration range of 0.65–5 mg/ml
Antiviral activity	Possesses antiviral activity	Possesses antiviral activity

genotoxicity, antioxidant, and antivirus activity. The main results of performed studies are summarized in Table 3.

Investigations of *cytotoxicity* on ST and MCF-7S cell lines showed that LSMO NPs had a constant maximum permissible concentration in contrast to Fe_3O_4 and it was higher (5.5 mg/ml) than the concentration of Fe_3O_4 particles (0.1–1.1 mg/ml).

Genotoxicity on NPs was investigated for magnetic fluids with the concentrations of Fe_3O_4 and LSMO, which were limited by the maximal nontoxic concentrations, established in the previous investigation of cytotoxicity. Performed studies showed that the magnetic fluid based on LSMO NPs *did not possess a genotoxic effect* on the ST and MCF-7S cell lines when Fe_3O_4 NPs in the concentration of 0.9 mg/ml displayed small genotoxic effect both on the ST and MCF-7S cell lines.

It was also established that both types of NPs possessed small *antiviral activity* in low concentrations. However, for LSMO NPs, this concentration was higher and equal 0.25–1.25 mg/ml.

As it is known, the growth of oncological tumors relates to chronic inflammation as well as with the presence of a high level of reactive oxygen species [22]. Therefore, investigations of the effect of magnetic NPs on the decreasing *the oxidative stress* were performed, and the presence of possible antioxidant properties was studied. Investigations were carried out on the ST cell line cultures, and they showed that Fe_3O_4 magnetite NPs could protect the cells from the oxidative stress in the concentrations of 1.1–1.4 mg/ml. However, as it was found out previously, such doses were already toxic for the cells. At the same time, LSMO manganite NPs possessed antioxidant properties in the concentrations of 0.65–5 mg/ml, which were nontoxic. Obtained data are very important since the main attention usually pays to the oxidative damage of magnetic NPs and not to their antioxidant activity.

The complex of performed cytological investigations described in [111] has shown that low cytotoxicity and genotoxicity of LSMO NPs make them more attractive for biological application compared to Fe_3O_4 NPs, which are characterized by higher toxicity. Moreover, LSMO NPs possess additional antioxidant activity in the quite wide concentration range that can be used in the different schemes of prevention and treatment.

At the same time, complex *in vitro* and *in vivo* investigations showed that LSMO NPs had low toxicity during the intratumoral injection and *did not cause the defection of the histological structure and functions of the main organs*. Therefore, they

can be used for performing further investigations as the heat mediators for magnetic hyperthermia.

Investigations of the toxicity of LSMO manganite NPs *in vivo* and their effect on the functioning animal organs were performed by authors [95, 97].

Acute toxicity of LSMO NPs was investigated on white mice of C57B1/6 line with the bodyweight of 20–22 g (each experimental group included six animals). The criteria of the toxicity were the death of animals in each group (in %), which was calculated according to the general methods that determined LD_{10}, LD_{50}, LD_{100}, etc. These parameters are defined as doses, where index means the percentage of dead animals, and maximum permissible dose, which does not lead to the death of any animal and does not cause the falling of the bodyweight more than 10%.

LSMO manganite NPs were injected into animals in such concentrations: 50, 100, 200, 300, and 400 mg per kg of body weight intraperitoneally and once in physiological solution. The duration of the investigations was 14 days. The loss of the bodyweight began at the dose of 200 mg/kg, but it was negligible and recovered just on the fourth day after the injection of NPs. The most significant weight loss was registered just on the first day after injection of NPs at the concentration of 300 mg/kg; however, animals gradually increased their weight on the second and third days, and the bodyweight of animals began to recover and even increase on the fourth day. The dose of 400 mg/kg caused the significant falling the body weight, and animals began to increase their weight gradually only on the seventh day after injection of NPs.

Obtained results indicate that maximum permissible dose for LSMO manganite equals 300 mg/kg of body weight and LD_{50}–1800 mg/kg of body weight.

Histological investigations were performed on the white rats with the Guerin carcinoma and on the mice of the C57B1/6 line with the Luice carcinoma of lungs. Morphological studies were carried out after 48 h of the injection of the nanocomposite. Any changes were not observed in the histological structure of the tumor (Guerin carcinoma in rats and Luice carcinoma in mice) as well as in normal organs such as liver, kidney, lungs, heart, and spleen after the injection of LSMO NPs in the dose of 300 mg/kg.

Investigations also showed that any toxic effect on the functions of the liver and kidneys was not present after the injection of LSMO nanocomposite into the tumor.

Complex *in vitro* and *in vivo* studies showed that LSMO NPs had low toxicity and did not cause the defection of the histological structure and functions of the main organs during the intratumoral injection. Therefore, they can be used for performing further investigations as the heat mediators for magnetic hyperthermia.

Further, in vivo investigations of the magnetic fluid based on the LSMO NPs as the heat mediators for magnetic hyperthermia were performed on the tumors of Guerin carcinoma and Volker carcinosarcomas [112]. Tumors were inculcated to the left and right thighs of the white rat, and the volume of the tumor was waited to reach the value of ~1 cm³. After that, magnetic fluid was injected into the tumor in the right thigh, and this tumor was subjected to the effect of an alternating magnetic field for 30 min (treatment was performed 1–2 times with the break of 1–2 days). The magnetic fluid was not injected into the tumor of the left thigh. It was used for comparison.
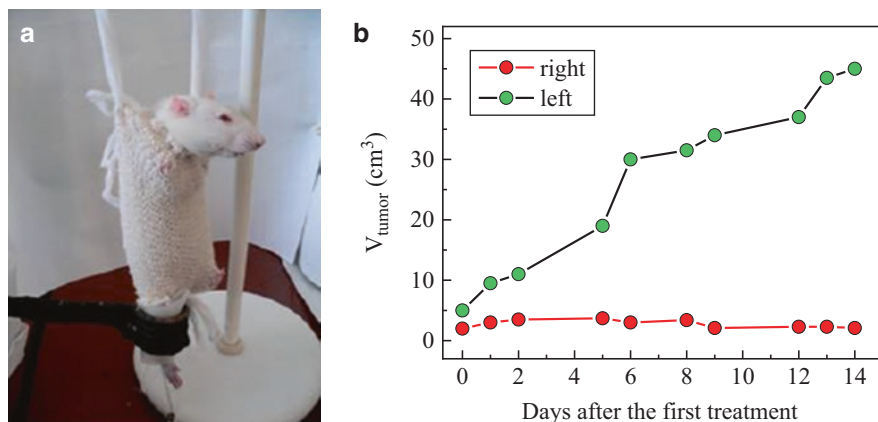
Fig. 14 (**a**) Experiments performing the magnetic hyperthermia on the previously inculcated tumor to the right thigh of the white rat; right thigh is placed into the coil of the generator of the alternating magnetic field. (**b**) Growth of the tumor of Guerin carcinoma in the right thigh after the injection of the magnetic fluid and the effect of the magnetic field (red curve) and nontreated tumor in the left thigh (black curve)

Such an approach led to the delay of the growth of the tumor in the right thigh; i.e., the volume of the tumor remained almost unchanged in contrast to the volume of the nontreated tumor (left thigh). The temperature in the tumor of the right thigh equaled in the average of 45–46.5 °C after the 30th minute of the heating.

The dependence of the efficiency of magnetic hyperthermia on the number of heating sessions was also established. In a series of experiments, heating was repeated for 3–4 times with the break of 2–3 days that led to the more significant decreasing the growth of tumor (Fig. 14): Volume of the tumor became 2.7 cm^3 on the 13th day after the first treatment, and volume of the nontreated tumors reached 47 cm^3. Increasing the volume of tumors was scarcely observed after the fourfold processing of the tumor with the magnetic fluid by the alternating magnetic field, and, in some cases, the regression of the tumor up to 35% was registered.

Performed investigations showed that the application of magnetic NPs of LSMO manganite in combination with the effect of the alternating magnetic field allows decreasing and even finishing the growth of oncological tumors after some time, and in the number of cases, it leads to the complete death of the tumor. This implies that LSMO NPs are promising materials for applications in magnetic hyperthermia.

8   Unresolved Issues and Prospects

Despite the recent progress in heat generating MNPs, there remain challenges to be addressed for the practical applications of magnetothermal effects of MNPs in biological systems. For example, the MNPs should be more precisely tailored to be biocompatible in physiological environments, ensuring the biosafety. For drug

release control or hyperthermia applications, the MNPs are needed to incorporate surface coating to have a prolonged blood half-life for the enhanced tissue-specific delivery [113–115]. For precise stimulation and regulation of cellular activities, fine controllability of local temperatures with the nanoscale spatial resolution is a critical factor, and thus, new methods to measure absolute temperature and thermal gradient in the close vicinity of MNP surfaces are required. To address these issues, notable efforts have been made and should be further confirmed in terms of surface chemistries (e.g., stealth coating of PEG or zwitterions and conjugation of targeting molecules), nanobiosystem interaction studies (e.g., pharmacokinetics, biodistribution, and cellular uptake), and nanoscale temperature measuring techniques based on various chemical strategies (e.g., heat-responsive azo compound and fluorescent polymers) [113–115].

In principle, MNPs upon the incorporation of functional molecules (e.g., antibodies, chemotherapy drugs, siRNAs, aptamers, and cell-penetrating peptides) can be a versatile platform capable of the noninvasive, remote regulation of cellular activities with molecular-level specificity and without penetration depth limits. Based on these characteristic features, the nanoscale heating of MNPs holds great potential to extend the target from the single-cell level to the whole body for the better understanding and precise control of biological systems.

References

1. Cancer Tomorrow (n.d.). https://gco.iarc.fr/tomorrow/home. Accessed 9 May 2020.
2. K.W. Baumann, J.M. Baust, K.K. Snyder, J.G. Baust, R.G. van Buskirk, Characterization of pancreatic cancer cell thermal response to heat ablation or cryoablation. Technol. Cancer Res. Treat. **16**, 393–405 (2017). https://doi.org/10.1177/1533034616655658
3. K.F. Chu, D.E. Dupuy, Thermal ablation of tumors: Biological mechanisms and advances in therapy. Nat. Rev. Cancer **14**, 199–208 (2014). https://doi.org/10.1038/nrc3672
4. A.G. Belous, S.O. Solopan, Y.D. Stupin, B.S. Khomenko, L.L. Kovalenko, O.P. Fedorchuk, *Method of Synthesis of Nickel-Manganese-Zinc Spinel Ferrites for Microwave Applications*. Ukrainian Patent, No 123709 (2018)
5. A.G. Belous, E.D. Solovyova, S.O. Solopan, O.v. Yelenich, L.N. Bubnovskaya, S.P. Osinsky, Properties and potential applications of ferromagnetic nanostructures in medicine and microwave engineering. Solid State Phenom. **230**, 95–100 (2015). https://doi.org/10.4028/www.scientific.net/SSP.230.95
6. A.G. Belous, S.O. Solopan, O.V. Yelenich, A.I. Tovstolytkin, T.V. Kolodiazhnyi, S.P. Osinsky, L.N. Bubnovskaya, Nanoparticles of spinel and perovskite ferromagnets and prospects for their application in medicine. AIP Conf. Proc. **1627**, 13–18 (2014). https://doi.org/10.1063/1.4901650
7. A.G. Belous, A.I. Tovstolytkin, S.A. Solopan, Y.Y. Shlapa, O.P. Fedorchuk, Nanosized oxide magnetics: synthesis, properties, application. Ukr. Chem. J. **83**, 3–24 (2017)
8. D.S. Nikam, S.V. Jadhav, V.M. Khot, M.R. Phadatare, S.H. Pawar, Study of AC magnetic heating characteristics of $Co_{0.5}Zn_{0.5}Fe_2O_4$ nanoparticles for magnetic hyperthermia therapy. J. Magn. Magn. Mater. **349**, 208–213 (2014). https://doi.org/10.1016/j.jmmm.2013.08.039
9. M. Veverka, K. Závěta, O. Kaman, P. Veverka, K. Knížek, E. Pollert, M. Burian, P. Kašpar, Magnetic heating by silica-coated Co-Zn ferrite particles. J. Phys. D. Appl. Phys. **47**, 065503 (2014). https://doi.org/10.1088/0022-3727/47/6/065503

10. Z. Shaterabadi, G. Nabiyouni, M. Soleymani, Physics responsible for heating efficiency and self-controlled temperature rise of magnetic nanoparticles in magnetic hyperthermia therapy. Prog. Biophys. Mol. Biol. **133**, 9–19 (2018). https://doi.org/10.1016/j.pbiomolbio.2017.10.001

11. A. López-Ortega, M. Estrader, G. Salazar-Alvarez, A.G. Roca, J. Nogués, Applications of exchange coupled bi-magnetic hard/soft and soft/hard magnetic core/shell nanoparticles. Phys. Rep. **553**, 1–32 (2015). https://doi.org/10.1016/j.physrep.2014.09.007

12. Q. Song, Z.J. Zhang, Controlled synthesis and magnetic properties of bimagnetic spinel ferrite $CoFe_2O_4$ and $MnFe_2O_4$ nanocrystals with core-shell architecture. J. Am. Chem. Soc. **134**, 10182–10190 (2012). https://doi.org/10.1021/ja302856z

13. Q. Zhang, I. Castellanos-Rubio, R. Munshi, I. Orue, B. Pelaz, K.I. Gries, W.J. Parak, P. del Pino, A. Pralle, Model driven optimization of magnetic anisotropy of exchange-coupled core-shell ferrite nanoparticles for maximal hysteretic loss. Chem. Mater. **27**, 7380–7387 (2015). https://doi.org/10.1021/acs.chemmater.5b03261

14. D. Polishchuk, N. Nedelko, S. Solopan, A. Ślawska-Waniewska, V. Zamorskyi, A. Tovstolytkin, A. Belous, Profound interfacial effects in $CoFe_2O_4/Fe_3O_4$ and $Fe_3O_4/CoFe_2O_4$ core/shell nanoparticles. Nanoscale Res. Lett. **13**, 67 (2018). https://doi.org/10.1186/s11671-018-2481-x

15. A.I. Tovstolytkin, M.M. Kulyk, V.M. Kalita, S.M. Ryabchenko, V.O. Zamorskyi, O.P. Fedorchuk, S.O. Solopan, A.G. Belous, Nickel-zinc spinel nanoferrites: Magnetic characterization and prospects of the use in self-controlled magnetic hyperthermia. J. Magn. Magn. Mater. **473**, 422–427 (2019). https://doi.org/10.1016/j.jmmm.2018.10.075

16. I. Sharifi, H. Shokrollahi, S. Amiri, Ferrite-based magnetic nanofluids used in hyperthermia applications. J. Magn. Magn. Mater. **324**, 903–915 (2012). https://doi.org/10.1016/j.jmmm.2011.10.017

17. Soshin Chikazumi, *Physics of Ferromagnetism, 1997*. Google books (n.d.). https://books.google.com.ua/books?id=AZVfuxXF2GsC&printsec=frontcover&hl=uk&source=gbs_ge_summary_r&cad=0#v=onepage&q&f=false. Accessed 25 Mar 2020.

18. V.M. Kalita, A.I. Tovstolytkin, S.M. Ryabchenko, O.V. Yelenich, S.O. Solopan, A.G. Belous, Mechanisms of AC losses in magnetic fluids based on substituted manganites. Phys. Chem. Chem. Phys. **17**, 18087–18097 (2015). https://doi.org/10.1039/c5cp02822a

19. Y. Shlapa, M. Kulyk, V. Kalita, T. Polek, A. Tovstolytkin, J.-M. Greneche, S. Solopan, A. Belous, Iron-doped (La,Sr)MnO$_3$ manganites as promising mediators of self-controlled magnetic nanohyperthermia. Nanoscale Res. Lett. **11**, 24 (2016). https://doi.org/10.1186/s11671-015-1223-6

20. E. Pollert, O. Kaman, P. Veverka, M. Veverka, M. Marysko, K. Záveta, M. Kacenka, I. Lukes, P. Jendelová, P. Kaspar, M. Burian, V. Herynek, Core-shell La$_{(1-x)}$Sr$_{(x)}$MnO$_3$ nanoparticles as colloidal mediators for magnetic fluid hyperthermia. Philos. Trans. R. Soc. **368**, 4389 (2010). https://doi.org/10.1098/rsta.2010.0123

21. A.I. Tovstolytkin, Y.M. Lytvynenko, A.V. Bodnaruk, O.V. Bondar, V.M. Kalita, S.M. Ryabchenko, Y.Y. Shlapa, S.O. Solopan, A.G. Belous, Unusual magnetic and calorimetric properties of lanthanum-strontium manganite nanoparticles. J. Magn. Magn. Mater. **498**, 166088 (2020). https://doi.org/10.1016/j.jmmm.2019.166088

22. O. Shydlovska, N. Zholobak, S. Dybkova, S. Osinsky, L. Bubnovskaya, O. Yelenich, S. Solopan, A. Belous, Synthesis and comparative characteristics of biological activities of (La, Sr)MnO$_3$ and Fe_3O_4 nanoparticles. Eur. J. Nanomed. **9**, 33–43 (2017). De Gruyter. https://doi.org/10.1515/ejnm-2016-0028

23. S.L. Easo, P.V. Mohanan, Dextran stabilized iron oxide nanoparticles: Synthesis, characterization and in vitro studies. Carbohydr. Polym. **92**, 726–732 (2013). https://doi.org/10.1016/j.carbpol.2012.09.098

24. R. Qiao, C. Yang, M. Gao, Superparamagnetic iron oxide nanoparticles: From preparations to in vivo MRI applications. J. Mater. Chem. **19**, 6274–6293 (2009). https://doi.org/10.1039/b902394a

25. S. Stolnik, L. Illum, S.S. Davis, Long circulating microparticulate drug carriers. Adv. Drug Deliv. Rev. **64**, 290–301 (2012). https://doi.org/10.1016/j.addr.2012.09.029

26. R.Y. Hong, B. Feng, L.L. Chen, G.H. Liu, H.Z. Li, Y. Zheng, D.G. Wei, Synthesis, characterization and MRI application of dextran-coated Fe_3O_4 magnetic nanoparticles. Biochem. Eng. J. **42**, 290–300 (2008). https://doi.org/10.1016/j.bej.2008.07.009

27. Q.A. Pankhurst, N.T.K. Thanh, S.K. Jones, J. Dobson, Progress in applications of magnetic nanoparticles in biomedicine. J. Phys. D. Appl. Phys. **42**, 224001 (2009). https://doi.org/10.1088/0022-3727/42/22/224001

28. I.I. Kaneva, D.G. Krutogin, V.G. Andreev, L.M. Letuk, *Ferrite Materials and Components of Magnetoelectronics* (Laboratornyi praktikum, MISiS, Moskow, 2005)

29. L.A. Reznitskii, A.S. Guzei, Thermodynamic properties of alkaline earth Titanates, Zirconates, and Hafnates. Russ. Chem. Rev. **47**, 99–119 (1978). https://doi.org/10.1070/rc1978v047n02abeh002213

30. A.G. Belous, Y.V. Pashkova, O.I. Vunov, et al., Effect of processing conditions on the phase transformations, structure and magnetoresistive properties of $La_{0.7}Sr_{0.3}MnO_{3\pm\gamma}$ manganites. Ukr. Chem. J. **71**, 17–23 (2005)

31. O.V. Yelenich, S.O. Solopan, T.V. Kolodiazhnyi, J.M. Greneche, A.G. Belous, Synthesis of iron oxide nanoparticles by different methods and study of their properties. Solid State Phenom. **230**, 108–113 (2015). https://doi.org/10.4028/www.scientific.net/SSP.230.108

32. S.O. Solopan, Y.D. Fateev, A.G. Belous, Features of synthesis of weakly agglomerated Fe_3O_4 nanoparticles in microemulsions. Ukr. Chem. J. **78**, 3–8 (2012)

33. O.V. Yelenich, S.O. Solopan, V.V. Trachevskii, A.G. Belous, Synthesis and properties of AFe_2O_4 (A = Mn, Fe, Co, Ni, Zn) nanoparticles produced by deposition from diethylene glycol solution. Russ. J. Inorg. Chem. **58**, 901–905 (2013)

34. O.V. Yelenich, S.A. Solopan, M. Troschenkov Yu, A.G. Belous, Synthesis of weakly agglomerated nanoparticles based Fe_3O_4 and $CoFe_2O_4$ in non-aqueous solutions. Ukr. Chem. J. **78**, 11–15 (2012)

35. O.V. Yelenich, S.O. Solopan, A.G. Belous, Polyol synthesis and properties of AFe_2O_4 nanoparticles (A = Mn, Fe, Co, Ni, Zn) with spinel structure. Solid State Phenom. **200**, 149–155 (2013). https://doi.org/10.4028/www.scientific.net/SSP.200.149

36. O. Yelenich, S. Solopan, T. Kolodiazhnyi, Y. Tykhonenko, A. Tovstolytkin, A. Belous, Magnetic properties and AC losses in AFe_2O_4 (A = Mn, Co, Ni, Zn) nanoparticles synthesized from nonaqueous solution. J. Chem. **2015**, 532198 (2015). https://doi.org/10.1155/2015/532198

37. A.V. Nagornyi, M.V. Avdeev, O.V. Yelenich, S.O. Solopan, A.G. Belous, A.V. Shulenina, V.A. Turchenko, D.V. Soloviov, L.A. Bulavin, V.L. Aksenov, Structural aspects of $Fe_3O_4/CoFe_2O_4$ magnetic nanoparticles according to X-ray and neutron scattering. J. Surf. Invest. **12**, 737–743 (2018). https://doi.org/10.1134/S102745101804033X

38. Y. Shlapa, S. Solopan, O. Yelenich, V. Trachevskii, A. Belous, Synthesis of ferromagnetic $La_{1-x}Sr_xMnO_3$ nanoparticles by precipitation from diethylene glycol solution and their properties. J. Adv. Ceram. **5**, 197–203 (2016). https://doi.org/10.1007/s40145-016-0190-4

39. Y. Shlapa, S. Solopan, A. Belous, A. Tovstolytkin, Effect of synthesis method of $La_{1-x}Sr_xMnO_3$ manganite nanoparticles on their properties. Nanoscale Res. Lett. **13**, 1–7 (2018). https://doi.org/10.1186/s11671-017-2431-z

40. A.K. Ganguli, A. Ganguly, S. Vaidya, Microemulsion-based synthesis of nanocrystalline materials. Chem. Soc. Rev. **39**, 474–485 (2010)

41. S.A. Solopan, A.G. Belous, S.P. Osinsky, A.I. Tovstolytkin, Features of synthesis of nanomaterials based on the modified lanthanum-strontium manganites for the hyperthermia of tumors. Nanosyst. Nanomater. Nanotechnol. **8**, 775–786 (2010)

42. Y.Y. Shlapa, S.A. Solopan, A.G. Belous, Magnetothermic effect in core/shell nanocomposite $(La,Sr)MnO_3/SiO_2$. Theor. Exp. Chem. **54**, 92–98 (2018). https://doi.org/10.1007/s11237-018-9551-0

43. A.G. Belous, S.A. Solopan, O.V. Yelenich, Y.Y. Shlapa, S.P. Osinsky, Synthesis and properties of ferromagnetic nanostructures and their possible application in medicine and UHF

technic, in *Fundamental Problems of Development of Novel Materials and Compounds of Chemical Production*, (2016), pp. 91–101

44. S.A. Solopan, A.V. Yelenich, A.I. Tovstolytkin, A.G. Belous, Effect of the features of synthesis of (La,Sr)MnO$_3$ nanoparticles on their properties. Nanosyst. Nanomater. Nanotechnol. **2**, 189–198 (2014)

45. Y.Y. Shlapa, S.O. Solopan, Y.V. Odynets, A.G. Belous, Organic-inorganic composite structures based on ferromagnetic (La,Sr)MnO$_3$ manganite nanoparticles. Ukr. Chem. J. **81**, 99–103 (2015)

46. S.O. Solopan, O.I. V'Yunov, A.G. Belous, T.I. Polek, A.I. Tovstolytkin, Effect of nanoparticles agglomeration on electrical properties of La$_{1-x}$A$_x$MnO$_3$ (A = Sr, Ba) nanopowder and ceramic solid solutions. Solid State Sci. **14**, 501–505 (2012). https://doi.org/10.1016/j.solidstatesciences.2012.01.030

47. O.V. Yelenich, S.O. Solopan, A.G. Belous, Synthesis of NiFe$_2$O$_4$ nanoparticles in non-aqueous solutions and their properties. Ukr. Chem. J. **79**, 3–8 (2013)

48. Y. Shlapa, S. Solopan, A. Belous, Nanoparticles of La$_{1-x}$Sr$_x$MnO$_3$ (0.23 ≤ x ≤ 0.25) manganite: Features of synthesis and crystallochemical properties. J. Magn. Magn. Mater. **510**, 166902 (2020)

49. Y. Shlapa, S. Solopan, A. Belous, Effect of mechano-chemical processing in the synthesis of weakly agglomerated ferromagnetic La$_{1-x}$Sr$_x$MnO$_3$ nanoparticles on their properties, in *2015 IEEE 35th International Conference on Electronics and Nanotechnology, ELNANO 2015 – Conference Proceedings*, (2015), pp. 282–286. https://doi.org/10.1109/ELNANO.2015.7146892

50. Y.T. He, S.J. Traina, Transformation of magnetite to goethite under alkaline pH conditions. Clay Miner. **42**, 13–19 (2007). https://doi.org/10.1180/claymin.2007.042.1.02

51. A.P. Khandhar, R.M. Ferguson, J.A. Simon, K.M. Krishnan, Enhancing cancer therapeutics using size-optimized magnetic fluid hyperthermia. J. Appl. Phys. **111**, 07B306 (2012). https://doi.org/10.1063/1.3671427

52. R. Hergt, W. Andrae, C.G. d'Ambly, I. Hilger, W.A. Kaiser, U. Richter, H.G. Schmidt, Physical limits of hyperthermia using magnetite fine particles. IEEE Trans. Magn. **34**, 3745–3754 (1998). https://doi.org/10.1109/20.718537

53. N.H. Cho, T.C. Cheong, J.H. Min, J.H. Wu, S.J. Lee, D. Kim, J.S. Yang, S. Kim, Y.K. Kim, S.Y. Seong, A multifunctional core-shell nanoparticle for dendritic cell-based cancer immunotherapy. Nat. Nanotechnol. **6**, 675–682 (2011). https://doi.org/10.1038/nnano.2011.149

54. S.H. Noh, W. Na, J.T. Jang, J.H. Lee, E.J. Lee, S.H. Moon, Y. Lim, J.S. Shin, J. Cheon, Nanoscale magnetism control via surface and exchange anisotropy for optimized ferrimagnetic hysteresis. Nano Lett. **12**, 3716–3721 (2012). https://doi.org/10.1021/nl301499u

55. P. Mélinon, S. Begin-Colin, J.L. Duvail, F. Gauffre, N.H. Boime, G. Ledoux, J. Plain, P. Reiss, F. Silly, B. Warot-Fonrose, Engineered inorganic core/shell nanoparticles. Phys. Rep. **543**, 163–197 (2014). https://doi.org/10.1016/j.physrep.2014.05.003

56. A.A. Sattar, H.M. El-Sayed, I. Alsuqia, Structural and magnetic properties of CoFe$_2$O$_4$/NiFe$_2$O$_4$ core/shell nanocomposite prepared by the hydrothermal method. J. Magn. Magn. Mater. **395**, 89–96 (2015). https://doi.org/10.1016/j.jmmm.2015.07.039

57. A.H. Habib, C.L. Ondeck, P. Chaudhary, M.R. Bockstaller, M.E. McHenry, Evaluation of iron-cobalt/ferrite core-shell nanoparticles for cancer thermotherapy. J. Appl. Phys. **103**, 07A307 (2008). https://doi.org/10.1063/1.2830975

58. R. Ghosh, L. Pradhan, Y.P. Devi, S.S. Meena, R. Tewari, A. Kumar, S. Sharma, N.S. Gajbhiye, R.K. Vatsa, B.N. Pandey, R.S. Ningthoujam, Induction heating studies of Fe$_3$O$_4$ magnetic nanoparticles capped with oleic acid and polyethylene glycol for hyperthermia. J. Mater. Chem. **21**, 13388–13398 (2011). https://doi.org/10.1039/c1jm10092k

59. O.V. Yelenich, S.O. Solopan, J.M. Greneche, A.G. Belous, Synthesis and properties MFe$_2$O$_4$ (M = Fe, Co) nanoparticles and core-shell structures. Solid State Sci. **46**, 19–26 (2015). https://doi.org/10.1016/j.solidstatesciences.2015.05.011

60. S.O. Solopan, N. Nedelko, S. Lewińska, A. Ślawska-Waniewska, V.O. Zamorskyi, A.I. Tovstolytkin, A.G. Belous, Core/shell architecture as an efficient tool to tune DC magnetic parameters and AC losses in spinel ferrite nanoparticles. J. Alloys Compd. **788**, 1203–1210 (2019). https://doi.org/10.1016/j.jallcom.2019.02.276

61. G. Franceschin, T. Gaudisson, N. Menguy, B.C. Dodrill, N. Yaacoub, J.-M. Grenèche, R. Valenzuela, S. Ammar, Exchange-biased $Fe_{3-x}O_4$-CoO granular composites of different morphologies prepared by seed-mediated growth in polyol: From core-shell to multicore embedded structures. Part. Part. Syst. Charact. **35**, 1800104 (2018). https://doi.org/10.1002/ppsc.201800104

62. N. Flores-Martinez, G. Franceschin, T. Gaudisson, P. Beaunier, N. Yaacoub, J.-M. Grenèche, R. Valenzuela, S. Ammar, Giant exchange-bias in polyol-made $CoFe_2O_4$-CoO core-shell like nanoparticles. Part. Part. Syst. Charact. **35**, 1800290 (2018). https://doi.org/10.1002/ppsc.201800290

63. T. Gaudisson, R. Sayed-Hassan, N. Yaacoub, G. Franceschin, S. Nowak, J.M. Grenèche, N. Menguy, P. Sainctavit, S. Ammar, On the exact crystal structure of exchange-biased Fe_3O_4-CoO nanoaggregates produced by seed-mediated growth in polyol. CrystEngComm **18**, 3799–3807 (2016). https://doi.org/10.1039/c6ce00700g

64. O. Masala, D. Hoffman, N. Sundaram, K. Page, T. Proffen, G. Lawes, R. Seshadri, Preparation of magnetic spinel ferrite core/shell nanoparticles: Soft ferrites on hard ferrites and vice versa. Solid State Sci. **8**, 1015–1022 (2006). https://doi.org/10.1016/j.solidstatesciences.2006.04.014

65. U.M. Engelmann, C. Shasha, E. Teeman, I. Slabu, K.M. Krishnan, Predicting size-dependent heating efficiency of magnetic nanoparticles from experiment and stochastic Néel-Brown Langevin simulation. J. Magn. Magn. Mater. **471**, 450–456 (2019). https://doi.org/10.1016/j.jmmm.2018.09.041

66. J. Carrey, B. Mehdaoui, M. Respaud, Simple models for dynamic hysteresis loop calculations of magnetic single-domain nanoparticles: Application to magnetic hyperthermia optimization. J. Appl. Phys. **109**, 083921 (2011). https://doi.org/10.1063/1.3551582

67. S. Chikazumi, C.D. (Chad D.) Graham, S. Chikazumi, *Physics of Ferromagnetism* (Oxford University Press, 1997). https://global.oup.com/academic/product/physics-of-ferromagnetism-9780198517764?cc=ua&lang=en&. Accessed 27 May 2019.

68. J.H. Lee, Y.M. Huh, Y.W. Jun, J.W. Seo, J.T. Jang, H.T. Song, S. Kim, E.J. Cho, H.G. Yoon, J.S. Suh, J. Cheon, Artificially engineered magnetic nanoparticles for ultra-sensitive molecular imaging. Nat. Med. **13**, 95–99 (2007). https://doi.org/10.1038/nm1467

69. C.N. Chinnasamy, A. Narayanasamy, N. Ponpandian, K. Chattopadhyay, K. Shinoda, B. Jeyadevan, K. Tohji, K. Nakatsuka, T. Furubayashi, I. Nakatani, Mixed spinel structure in nanocrystalline $NiFe_2O_4$. Phys. Rev. B Condens. Matter Mater. Phys. **63**, 184108 (2001). https://doi.org/10.1103/PhysRevB.63.184108

70. M. Sanna Angotzi, V. Mameli, C. Cara, A. Musinu, C. Sangregorio, D. Niznansky, H.L. Xin, J. Vejpravova, C. Cannas, Coupled hard-soft spinel ferrite-based core-shell nanoarchitectures: Magnetic properties and heating abilities. Nanoscale Adv. **2**, 3191–3201 (2020). https://doi.org/10.1039/d0na00134a

71. O.V. Yelenich, S.O. Solopan, T.V. Kolodiazhnyi, V.V. Dzyublyuk, A.I. Tovstolytkin, A.G. Belous, Magnetic properties and high heating efficiency of $ZnFe_2O_4$ nanoparticles. Mater. Chem. Phys. **146**, 129–135 (2014). https://doi.org/10.1016/j.matchemphys.2014.03.010

72. P. Gao, X. Hua, V. Degirmenci, D. Rooney, M. Khraisheh, R. Pollard, R.M. Bowman, E.V. Rebrov, Structural and magnetic properties of $Ni_{1-x}Zn_xFe_2O_4$ (x=0, 0.5 and 1) nanopowders prepared by sol-gel method. J. Magn. Magn. Mater. **348**, 44–50 (2013). https://doi.org/10.1016/j.jmmm.2013.07.060

73. C. Srinivas, B.V. Tirupanyam, A. Satish, V. Seshubai, D.L. Sastry, O.F. Caltun, Effect of Ni^{2+} substitution on structural and magnetic properties of Ni-Zn ferrite nanoparticles. J. Magn. Magn. Mater. **382**, 15–19 (2015). https://doi.org/10.1016/j.jmmm.2015.01.008

74. A.H. Morr, K. Haneda, Magnetic structure of small NiFe^{2}O^4 particles. J. Appl. Phys. **52**, 2496–2498 (1981). https://doi.org/10.1063/1.328979

75. B.T. Naughton, D.R. Clarke, Lattice expansion and saturation magnetization of nickel–zinc ferrite nanoparticles prepared by aqueous precipitation. J. Am. Ceram. Soc. **90**, 3541–3546 (2007). https://doi.org/10.1111/j.1551-2916.2007.01980.x

76. N. Daffé, F. Choueikani, S. Neveu, M.A. Arrio, A. Juhin, P. Ohresser, V. Dupuis, P. Sainctavit, Magnetic anisotropies and cationic distribution in CoFe$_2$O$_4$ nanoparticles prepared by co-precipitation route: Influence of particle size and stoichiometry. J. Magn. Magn. Mater. **460**, 243–252 (2018). https://doi.org/10.1016/j.jmmm.2018.03.041

77. R.R. Wildeboer, P. Southern, Q.A. Pankhurst, On the reliable measurement of specific absorption rates and intrinsic loss parameters in magnetic hyperthermia materials. J. Phys. D. Appl. Phys. **47**, 495003 (2014). https://doi.org/10.1088/0022-3727/47/49/495003

78. A. Urushibara, Y. Moritomo, T. Arima, A. Asamitsu, G. Kido, Y. Tokura, Insulator-metal transition and giant magnetoresistance in La$_{1-x}$Sr$_x$MnO$_3$. Phys. Rev. B **51**, 14103–14109 (1995). https://doi.org/10.1103/PhysRevB.51.14103

79. A.G. Belous, O.I. V'yunov, E.V. Pashkova, O.Z. Yanchevskii, A.I. Tovstolytkin, A.M. Pogorelyi, Effects of chemical composition and sintering temperature on the structure of La$_{1-x}$Sr$_x$MnO$_{3 \pm \gamma}$ solid solutions. Inorg. Mater. **39**, 161–170 (2003). https://doi.org/10.1023/A:1022198613723

80. D.H. Manh, P.T. Phong, P.H. Nam, D.K. Tung, N.X. Phuc, I.J. Lee, Structural and magnetic study of La$_{0.7}$Sr$_{0.3}$MnO$_3$ nanoparticles and AC magnetic heating characteristics for hyperthermia applications. Phys. B Condens. Matter **444**, 94–102 (2014). https://doi.org/10.1016/j.physb.2014.03.025

81. Y. Shlapa, I. Timashkov, S. Solopan, M. Rajnak, J. Kovac, M. Molcan, M. Timko, A. Belous, Ce-doped manganites of lanthanum-strontium as promising inducers of magnetic hyperthermia, in *IEEE 39th International Conference on Electronics and Nanotechnology, ELNANO 2019*, (2019), pp. 439–433

82. I.P. Timashkov, Y.Y. Shlapa, S.A. Solopan, A.G. Belous, Synthesis and crystallochemical properties of cerium-substituted (La,Sr)MnO$_3$ manganite nanoparticles. Ukr. Chem. J. **85**, 17–24 (2019). Ukrainian Chemical, Institute of General and Inorganic Chemistry named after V.I. Vernadsky NAS of Ukraine. https://doi.org/10.33609/0041-6045.85.9.2019.17-24

83. Y. Shlapa, S. Solopan, A. Bodnaruk, M. Kulyk, V. Kalita, Y. Tykhonenko-Polishchuk, A. Tovstolytkin, A. Belous, Effect of synthesis temperature on structure and magnetic properties of (La, Nd)$_{0.7}$Sr$_{0.3}$MnO$_3$ nanoparticles. Nanoscale Res. Lett. **12**, 1–7 (2017). https://doi.org/10.1186/s11671-017-1884-4

84. Y. Shlapa, S. Solopan, A. Bodnaruk, M. Kulyk, V. Kalita, Y. Tykhonenko-Polishchuk, A. Tovstolytkin, V. Zinchenko, A. Belous, Lanthanum-strontium manganites for magnetic nanohyperthermia: Fine tuning of parameters by substitutions in lanthanum sublattice. J. Alloys Compd. **702**, 31–37 (2017). https://doi.org/10.1016/j.jallcom.2017.01.222

85. T.I. Polek, A.I. Tovstolytkin, M.M. Kulyk, Y.Y. Shlapa, S.O. Solopan, A.G. Belous, Crystallographic, magnetic and magnetoresistive properties of La$_{0.77}$Sr$_{0.23}$Mn$_{1-y}$Fe$_y$O$_3$ ceramics. Metalophys. Novel Technol. **38**, 479–492 (2016)

86. B. Hildebrandt, P. Wust, O. Ahlers, A. Dieing, G. Sreenivasa, T. Kerner, R. Felix, H. Riess, The cellular and molecular basis of hyperthermia. Crit. Rev. Oncol. Hematol. **43**, 33–56 (2002). https://doi.org/10.1016/S1040-8428(01)00179-2

87. S. Vasseur, E. Duguet, J. Portier, G. Goglio, S. Mornet, E. Hadová, K. Knížek, M. Maryško, P. Veverka, E. Pollert, Erratum to "Lanthanum manganese perovskite nanoparticles as possible in vivo mediators for magnetic hyperthermia". J. Magn. Magn. Mater. **307**, 330 (2006). https://doi.org/10.1016/j.jmmm.2006.06.034

88. N.K. Prasad, K. Rathinasamy, D. Panda, D. Bahadur, TC-tuned biocompatible suspension of La$_{0.73}$Sr$_{0.27}$MnO$_3$ for magnetic hyperthermia. J. Biomed. Mater. Res. B Appl. Biomater. **85B**, 409–416 (2008). https://doi.org/10.1002/jbm.b.30959

89. A.K. Pradhan, R. Bah, R.B. Konda, R. Mundle, H. Mustafa, O. Bamiduro, R.R. Rakhimov, X. Wei, D.J. Sellmyer, Synthesis and magnetic characterizations of manganite-based composite nanoparticles for biomedical applications. J. Appl. Phys. **103**, 07F704 (2008). https://doi.org/10.1063/1.2829906

90. E. Pollert, K. Knížek, M. Maryško, P. Kašpar, S. Vasseur, E. Duguet, New T_c-tuned magnetic nanoparticles for self-controlled hyperthermia. J. Magn. Magn. Mater. **316**, 122–125 (2007). https://doi.org/10.1016/j.jmmm.2007.02.031

91. A. Belous, A. Tovstolytkin, S. Solopan, Y. Shlapa, O. Fedorchuk, Synthesis, properties and applications of some magnetic oxide based nanoparticles and films. Acta Phys. Polon. **A133**, 1006 (2018). https://doi.org/10.12693/APhysPolA.133.1006

92. K. Zhang, T. Holloway, J. Pradhan, M. Bahoura, R. Bah, R.R. Rakhimov, A.K. Pradhan, R. Prabakaran, G.T. Ramesh, Synthesis and magnetic characterizations of $La_{1-x}Sr_xMnO_3$ nanoparticles for biomedical applications. J. Nanosci. Nanotechnol. **10**, 5520–5526 (2010). https://doi.org/10.1166/jnn.2010.2437

93. A. Belous, S. Solopan, A. Yelenich, L. Bubnovskaya, S. Osinsky, Nanoparticles of ferromagnetic materials and possibilities of their application in the hyperthermia of malignant tumors, in *2013 IEEE 33rd International Scientific Conference Electronics and Nanotechnology, ELNANO 2013 – Conference Proceedings*, (2013), pp. 280–284. https://doi.org/10.1109/ELNANO.2013.6552060

94. A.I. Tovstolytkin, Y.Y. Shlapa, S.O. Solopan, A.V. Bodnaruk, M.M. Kulyk, V.M. Kalita, V.O. Zamorskyi, S.M. Ryabchenko, A.G. Belous, Manganite nanoparticles as promising heat mediators for magnetic hyperthermia: Comparison of different chemical substitutions. Acta Phys. Pol. A **133**, 1017–1020 (2018)

95. L. Bubnovskaya, A. Belous, A. Solopan, A. Podoltsev, I. Kondratenko, A. Kovelskaya, T. Sergienko, S. Osinsky, Nanohyperthermia of malignant tumors. II. in vivo tumor heating with manganese perovskite nanoparticles. Exp. Oncol. **34**, 336–339 (2012)

96. L. Bubnovskaya, A. Belous, S. Solopan, A. Kovelskaya, L. Bovkun, A. Podoltsev, I. Kondtratenko, S. Osinsky, Magnetic fluid hyperthermia of rodent tumors using manganese perovskite nanoparticles. J. Nanopart. **2014**, 1–9 (2014). https://doi.org/10.1155/2014/278761

97. S. Solopan, A. Belous, A. Yelenich, L. Bubnovskaya, A. Kovelskaya, A. Podoltsev, I. Kondratenko, S. Osinsky, Nanohyperthermia of malignant tumors. I. Lanthanum-strontium manganite magnetic fluid as potential inducer of tumor hyperthermia. Exp. Oncol. **33**, 130–135 (2011)

98. O.V. Yelenich, S.O. Solopan, T.V. Kolodiazhnyi, V.V. Dzyublyuk, A.I. Tovstolytkin, A.G. Belous, Superparamagnetic behavior and AC-losses in $NiFe_2O_4$ nanoparticles. Solid State Sci. **20**, 115–119 (2013). https://doi.org/10.1016/j.solidstatesciences.2013.03.013

99. A. Jordan, R. Scholz, P. Wust, H. Fähling, R. Felix, Magnetic fluid hyperthermia (MFH): Cancer treatment with AC magnetic field induced excitation of biocompatible superparamagnetic nanoparticles. J. Magn. Magn. Mater. **201**, 413–419 (1999). https://doi.org/10.1016/S0304-8853(99)00088-8

100. R. Hergt, S. Dutz, R. Müller, M. Zeisberger, Magnetic particle hyperthermia: nanoparticle magnetism and materials development for cancer therapy. J. Phys. Condens. Matter **18**, S2919–S2934 (2006). https://doi.org/10.1088/0953-8984/18/38/S26

101. R.E. Rosensweig, Heating magnetic fluid with alternating magnetic field. J. Magn. Magn. Mater. **252**, 370–374 (2002). https://doi.org/10.1016/S0304-8853(02)00706-0

102. S. Dutz, R. Hergt, Magnetic particle hyperthermia—A promising tumour therapy? Nanotechnology **25**, 452001 (2014). https://doi.org/10.1088/0957-4484/25/45/452001

103. S. Bedanta, W. Kleemann, Supermagnetism. J. Phys. D. Appl. Phys. **42**, 013001 (2009). https://doi.org/10.1088/0022-3727/42/1/013001

104. B. Mehdaoui, A. Meffre, J. Carrey, S. Lachaize, L.-M. Lacroix, M. Gougeon, B. Chaudret, M. Respaud, Optimal size of nanoparticles for magnetic hyperthermia: A combined theoretical and experimental study. Adv. Funct. Mater. **21**, 4573–4581 (2011). https://doi.org/10.1002/adfm.201101243

105. D.M. Polishchuk, Y.O. Tykhonenko-Polishchuk, S.O. Solopan, A.V. Bodnaruk, M.M. Kulyk, A.I. Tovstolytkin, A.M. Pogorily, Features of the magnetic state of ensembles of nanoparticles of substituted manganites: Experiment and model calculations. Low Temp. Phys. **43**, 570–577 (2017)

106. A.V. Bodnaruk, V.M. Kalita, M.M. Kulyk, S.M. Ryabchenko, A.I. Tovstolytkin, S.O. Solopan, A.G. Belous, Critical behavior of ensembles of superparamagnetic nanoparticles with dispersions of magnetic parameters. J. Phys. Condens. Matter **31**, 375801 (2019). https://doi.org/10.1088/1361-648X/ab26fa

107. V.M. Kalita, D.M. Polishchuk, D.G. Kovalchuk, A.V. Bodnaruk, S.O. Solopan, A.I. Tovstolytkin, S.M. Ryabchenko, A.G. Belous, Interplay between superparamagnetic and blocked behavior in an ensemble of lanthanum-strontium manganite nanoparticles. Phys. Chem. Chem. Phys. **19**, 27015–27024 (2017). https://doi.org/10.1039/c7cp05547a

108. A.V. Nagornyi, V.I. Petrenko, M.V. Avdeev, O.V. Yelenich, S.O. Solopan, A.G. Belous, A.Y. Gruzinov, O.I. Ivankov, L.A. Bulavin, Structural aspects of magnetic fluid stabilization in aqueous agarose solutions. J. Magn. Magn. Mater. **431**, 16–19 (2017). https://doi.org/10.1016/j.jmmm.2016.10.018

109. N. Singh, G.J.S. Jenkins, R. Asadi, S.H. Doak, Potential toxicity of superparamagnetic iron oxide nanoparticles (SPION). Nano Rev. **1**, 5358 (2010). https://doi.org/10.3402/nano.v1i0.5358

110. S. Pecorini, L. Gibellini, S. de Biasi, E. Bianchini, M. Nasi, A. Cossarizza, M. Pinti, Mitochondria, oxidative stress, cancer, and aging, in *Geriatric Oncology*, ed. by M. Extermann, (Springer International Publishing, Cham, 2020), pp. 183–204. https://doi.org/10.1007/978-3-319-57415-8_80

111. L. Bubnovskaya, N. Lukyanova, A. Belous, S. Solopan, Y. Shlapa, A. Podoltsev, Some effects of nanohyperthermia on the basis of lanthanum-strontium manganites (La,Sr)MnO$_3$ nanoparticles as heating mediators. Acta Sci. Cancer Biol. **4**, 1–8 (2020)

112. O. Veiseh, J.W. Gunn, M. Zhang, Design and fabrication of magnetic nanoparticles for targeted drug delivery and imaging. Adv. Drug Deliv. Rev. **62**, 284–304 (2010). https://doi.org/10.1016/j.addr.2009.11.002

113. W. Lin, Introduction: Nanoparticles in medicine. Chem. Rev. **115**, 10407–10409 (2015). https://doi.org/10.1021/acs.chemrev.5b00534

114. L. Polo-Corrales, C. Rinaldi, et al., J. Appl. Phys. **111**, 07B334 (2012). https://doi.org/10.1063/1.3680532

115. A. Riedinger, P. Guardia, A. Curcio, M.A. Garcia, R. Cingolani, L. Manna, T. Pellegrino, Subnanometer local temperature probing and remotely controlled drug release based on Azo-functionalized iron oxide nanoparticles. Nano Lett. **13**, 2399–2406 (2013). https://doi.org/10.1021/nl400188q